metals

MDPI

Article

Dislocation Loop Generation Differences between Thin Films and Bulk in EFDA Pure Iron under Self-Ion Irradiation at 20 MeV

Marcelo Roldán [1,2,*], Fernando José Sánchez [1,3], Pilar Fernández [1], Christophe J. Ortiz [1], Adrián Gómez-Herrero [3] and David Jiménez Rey [1]

[1] CIEMAT, National Fusion Laboratory, Technology Division, Avda. Complutense, 40, 28040 Madrid, Spain; fernandojose.sanchez@ciemat.es (F.J.S.); pilar.fernandez@ciemat.es (P.F.); christophe.ortiz@ciemat.es (C.J.O.); d.jimenez@ciemat.es (D.J.R.)

[2] CMAM, Centre from Micro Analysis of Materials, C/Faraday 3, Universidad Autónoma de Madrid, Campus de Cantoblanco, 28049 Madrid, Spain

[3] National Center from Electron Microscopy, 28040 Madrid, Spain; adriangh@pdi.ucm.es

* Correspondence: marcelo.roldan@ciemat.es

Abstract: In the present investigation, high-energy self-ion irradiation experiments (20 MeV Fe^{+4}) were performed on two types of pure Fe samples to evaluate the formation of dislocation loops as a function of material volume. The choice of model material, namely EFDA pure Fe, was made to emulate experiments simulated with computational models that study defect evolution. The experimental conditions were an ion fluence of 4.25 and 8.5 $\times$ 10^{15} ions/cm^2 and an irradiation temperature of 350 and 450 °C, respectively. First, the ions pass through the samples, which are thin films of less than 100 nm. With this procedure, the formation of the accumulated damage zone, which is the peak where the ions stop, and the injection of interstitials are prevented. As a result, the effect of two free surfaces on defect formation can be studied. In the second type of experiments, the same irradiations were performed on bulk samples to compare the creation of defects in the first 100 nm depth with the microstructure found in the whole thickness of the thin films. Apparent differences were found between the thin foil irradiation and the first 100 nm in bulk specimens in terms of dislocation loops, even with a similar primary knock-on atom (PKA) spectrum. In thin films, the most loops identified in all four experimental conditions were b $\pm a_0$<100>{200} type with sizes of hundreds of nm depending on the experimental conditions, similarly to bulk samples where practically no defects were detected. These important results would help validate computational simulations about the evolution of defects in alpha iron thin films irradiated with energetic ions at large doses, which would predict the dislocation nucleation and growth.

Keywords: irradiation damage characterisation; thin films; dislocation loops; transmission electron microscopy

check for updates

Citation: Roldán, M.; Sánchez, F.J.; Fernández, P.; Ortiz, C.J.; Gómez-Herrero, A.; Rey, D.J. Dislocation Loop Generation Differences between Thin Films and Bulk in EFDA Pure Iron under Self-Ion Irradiation at 20 MeV. *Metals* **2021**, *11*, 2000. https://doi.org/10.3390/met11122000

Academic Editor: Vladimír Slugeň

Received: 3 October 2021
Accepted: 6 December 2021
Published: 10 December 2021

Publisher's Note: MDPI stays neutral with regard to jurisdictional claims in published maps and institutional affiliations.

Copyright: © 2021 by the authors. Licensee MDPI, Basel, Switzerland. This article is an open access article distributed under the terms and conditions of the Creative Commons Attribution (CC BY) license (https://creativecommons.org/licenses/by/4.0/).

1. Introduction

Nowadays, one of the most critical challenges in the development of fusion energy is to predict and mitigate the effects of significant levels of transmuted gas atoms (He and H) along with the high displacement damage produced by high-energy neutrons that affect the mechanical properties of the structural materials and gives rise to phenomena such as swelling. Many issues related to irradiation defects are still unknown. Understanding the macroscopic effects of loops due to irradiation on structural materials requires further research at different levels: experimental observations by transmission electron microscopy (TEM) in basic and straightforward metals such as model alloys will be helpful as a validation tool for modelling.

The computational modelling of radiation damage in fusion materials may help predict the damage effects, how to mitigate these effects and contribute to the design of a

demonstration fusion power plant (DEMO) [1] in the medium term. Modelling would help understand the damage underlying physical mechanisms and predict their evolution along the reactor lifetime. The new models and computational codes must be validated with experiments to achieve a robust computational approach. There are three ways of analysing irradiation defects with a TEM which are in situ TEM on thin films [2–8], ex situ irradiated thin films [9], and ex situ irradiated bulk, also called post-mortem experiments [10–13].

This research was carried out to advance the development of computer-solved physical models that simulate the evolution of the defects generated by irradiation and their interaction with all the other factors involved, such as alloying elements and other dislocations that present precipitates, among others. Nowadays, the available models are not multiscale, but different methods and codes depend on the desired result, accuracy, and available computing power [14]. From the point of view of defect evolution, the most common is Object kinetic Monte Carlo (O-KMC) which allows parallel work using state-of-the-art graphics cards. It is expected that, in the short term, the gap between these models, which study the dynamics of dislocations at a larger scale, will be eliminated and will eventually be able to be coupled to more common codes of structural calculations using finite elements. However, regardless of the simulated physics, it is always necessary to validate both the physics implemented in these codes and the efficiency while the code operates. For this, it is necessary to have experimental results obtained from experiments developed to support the modelling investigations, not only to obtain experimental results.

Furthermore, it is necessary to consider all the parameters that can influence the development of the experiment to determine which are quantifiable and controllable (furnace temperature, sample preparation, irradiation area, beam energy, and current) and to always maintain these systematics. From a scientific point of view, working with some uncertainty in the results is valid. However, computational scientists require greater accuracy.

In this case, these experiments were performed to obtain more information regarding the effect on defects generated by irradiation in thin films. The irradiated samples have two free surfaces that act as defect sinks and are a source of vacancies, affecting the evolution of dislocation loops [15–17]. With an increase in dose, irradiation temperature, and, especially, avoiding the depth where self-interstitial atoms (SIAs) were injected into the material by irradiating with very energetic ions that have a very low probability of collision with lattice atoms, so the damage profile is more similar to that of neutrons.

The structural materials that will be part of the future nuclear fusion reactor will have to withstand an extremely aggressive environment for as long as possible. Developing steel that maintains its structural integrity against this environment, characterised by high temperature, cyclic loading, and 14 MeV neutron radiation, is a considerable challenge for the scientific community [1,18]. Two routes have been established which, although independent, are necessary to reach the final goal. On the one hand, the experimental route, which, based on the vast knowledge of the effects of radiation on materials mainly used in fission reactors, has managed to materialise steels with good properties against radiation in terms of structural stability, corrosion, and radiation resistance [19,20], but to date lack a scenario similar to that of the future fusion reactor in which to study the effect of neutron damage. On the other hand, the development of computational models that simulate the effects of radiation allows the development of experiments with other damage techniques, such as ion beams [21] or fast neutrons that emulate neutron damage.

However, to predict the evolution of materials and thus their microstructure, a profound understanding of the physics of irradiation damage is necessary. In addition, computational scientists must rely on results from experiments designed for this purpose, allowing them to validate the physics implemented in these models. Moreover, it is with this objective in mind that this research was carried out.

From the point of view of the study of the evolution of irradiation defects in materials, being able to observe how they are generated, how they interact with each other, growing or disappearing through in situ TEM studies [6,7,22] allows us to have a dynamic interpretation of the defect fate. On the other hand, the results obtained from the more conventional

studies called post-mortem (studied when irradiation ends) only represent the photo finish of the microstructural evolution. However, there is a fundamental difference between the two; the sample volume subjected to the radiation is radically different: a few nanometres (less than 100 nm) for thin films and a semi-infinite material in bulk in terms of thickness.

Regarding the energy of the ions, to prevent the effect of the injection of self-interstitial atoms into the material in thin films, as well as to move the braking peak away from the surface in bulk samples, 20 MeV Fe ions were used. Comparing the damage generated in the thin films and the first 100 nm of the FIB lamellae extracted from the bulk specimens, it was observed that both microstructural developments were utterly different. For this reason, the in-depth study was focused on understanding and explaining the reasons for such a high generation of dislocation loops even when the probability of kinetic energy transfer by the incident ion to the atoms forming the sample is very low. In probabilistic terms, this means that most irradiated ions transfer very little energy to the lattice, i.e., the film should be transparent. However, the results indicate the opposite.

2. Experimental Procedure

2.1. Material

The material used for this research was a very pure iron provided by the European Fusion Development Agreement (EFDA now EUROfusion) and manufactured by the École Nationale Supérieure des Mines (ARMINES), Paris, France [23]. Its composition and microstructural characteristics are the following. Firstly, the average grain size was 183 µm, but grains between 4 and 650 µm were also found. Secondly, the initial dislocation density provided by the manufacturer was 1.8×10^8 cm^{-2} (non-homogenously distributed). However, a higher dislocation density, of 1.44×10^{10} cm^{-2}, was calculated after the conventional sample preparation route. Finally, no secondary phases within the matrix were observed. Further details about the dislocation microstructure can be found in Table 1, below [24].

Table 1. Chemical composition of pure EFDA Fe manufactured by ARMINES.

	C	S	O	N	P	Cr
(wt ppm)	4.3	1.3	4	3.6	0.03	0.03

Before irradiation, 3 mm discs were prepared following the conventional route for metal specimens for TEM observations. First, the pure iron foil is thinned up to 100 µm so that the 3 mm discs can be punched out. Finally, the discs were electropolished with the Tenupol-5 (Struers) device, using a mixture of sulfuric acid and methanol (4:1) at RT and 9 V.

However, the inner characteristics of this electrolytic process generate a specimen with a gradual increase in thickness and a large electron transparent area (Figure 1a). However, it sometimes makes small smooth holes that allow us to analyse the sample far from the main thin area (Figure 1b).

2.2. Irradiation

Irradiations were performed in a Tandem accelerator with a terminal voltage of 5 MV with a Cockroft–Walton multiplier, placed at Universidad Autónoma de Madrid, Spain (CMAM). More details about the ion accelerator can be found in [21]. In every experiment, two specimens were simultaneously irradiated: one electropolished for thin-film studies and the other just superficially polished for bulk experiments. In addition, the beam quality and size were checked by the ionoluminescence signal [25] of some pieces of fused silica attached to the holder. Additionally, as the temperature is a critical parameter, it was controlled using a K-type thermocouple attached very close to the specimens to control the holder temperature (to double-check the temperature set-point in the controller). Figure 2 shows all of the features mentioned above conforming the set-up.

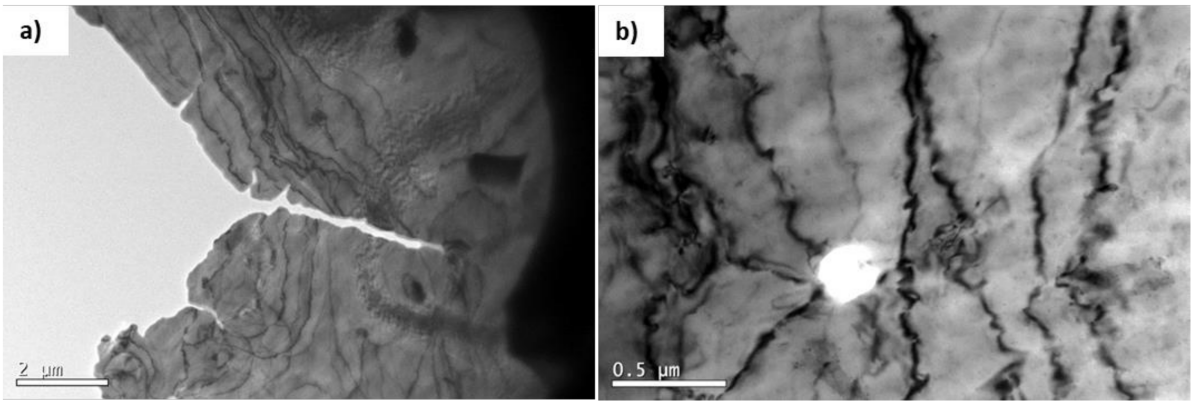


Figure 1. Pure EFDA Fe TEM micrograph showing the main hole and the transparent area after electropolishing with a large and homogeneous thin area (**a**) and a small smooth hole with an excellent electropolished volume irradiated (**b**).

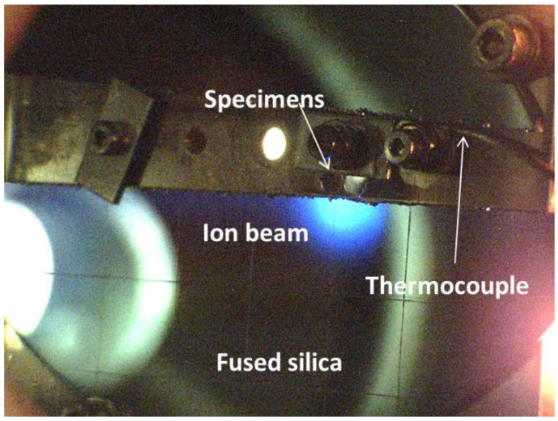


Figure 2. Sample holder shows the irradiated discs, with part of the beam hitting the fused silica (blue light). The image was taken with a considerable integration time to enhance contrast.

After checking the quality of the electropolished specimens, the irradiation took place as follows: using self-ions at 20 MeV, Fe^{+4} at two different fluences, 4.25×10^{15} ion/cm^2 and 8.53×10^{15} ion/cm^2, henceforth low dose (LD) and high dose (HD) and at two different irradiation temperatures of 300 and 450 °C, respectively. The corresponding damage at the Bragg peak was 5 and 10 dpa for the bulk specimens, as shown in Figure 3a, calculated by Stopping and Range of Ions in Matter (SRIM), using the method proposed in [26]. However, focusing on the first 200 nm, the dpa level dropped drastically to approximately 0.05 and 0.17 dpa, corresponding to the damage produced in the thin films, Figure 3b.

2.3. Sample Characterisation

Focus ion beam (FIB) lamellae were fabricated from the irradiated bulk specimens employing the lift-out technique, and their surface was cleaned with low Ar kV, using the Precision Ion Polishing System by Gatan (PIPS II) device [27]. The lamellae contained all the irradiation depth, but only the first 100 nm were studied since that depth corresponds to the thin film thickness. On the other hand, irradiated thin films were directly studied by transmission electron microscopy (TEM); only a plasma cleaning procedure was applied each time the samples were placed in the microscope to remove any organic residue.

The defect characterisation was performed with a JEOL 2100HT transmission electron microscope with a high tilt holder (±45°) at the Centro Nacional de Microscopía at Madrid (CNME).

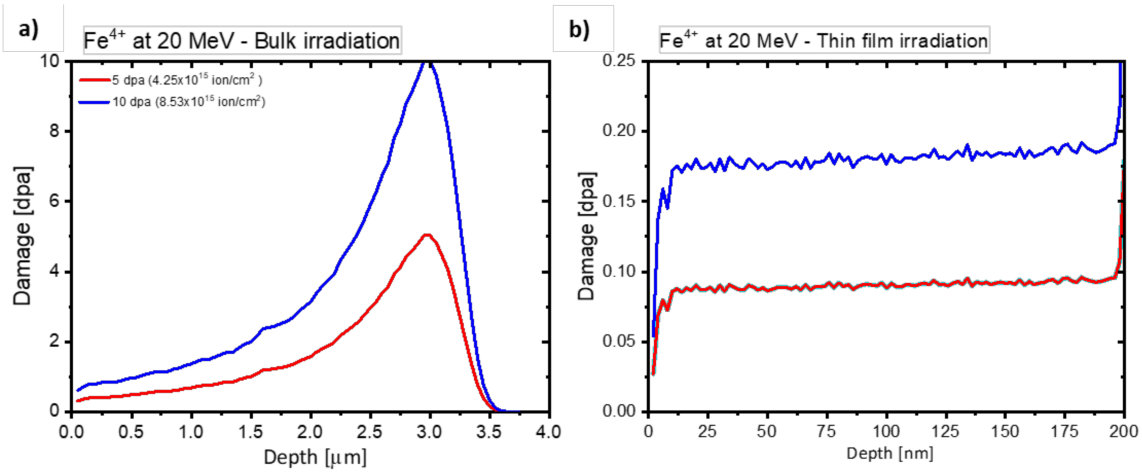


Figure 3. Damage profile for the fluences used in the experiments: low dose (LD), 4.25×10^{15} ion/cm^2, and high dose (HD), 8.53×10^{15} ion/cm^2, which correspond to the damage level at the peak of 5 and 10 dpa, respectively, (**a**), and the damage expected only in the first 200 nm for the same fluences, (**b**).

As previously mentioned, the main objective was to carry out a complete characterisation by TEM of the defects produced by the irradiation of very energetic iron ions when passing through thin films. These results will be compared to those obtained by analysing the defects found in the first 200 nm of irradiated bulk material. Due to the characteristics of the TEM itself and the time cost involved, it was essential to design an optimal methodology to carry out these studies.

First, an initial check of the four samples was carried out to validate the thin areas and detect possible oxide formation or some other type of surface degradation. Then, in the same way, the existence of any excessive dislocations that could have interfered with the evolution of the irradiation defects in any of the samples were quantitively evaluated.

Once the samples were checked, validating their condition for TEM analysis, a study of the size of the dislocation loops was carried out. This consideration is essential when one wants to determine the Burger vector, b, of these defects. This parameter represents the magnitude and direction of the lattice distortion induced by these defects. It can be determined by TEM because the dislocation is invisible to the microscope when b and the diffraction vector g are mutually perpendicular, i.e., when b lies in the diffraction planes of a crystal. More rigorously, the invisibility criterion is derived from the dynamic image theory of dislocation image contrast [28]. Tilting the sample in the TEM and satisfying several different diffraction conditions (i.e., different g-vectors) implies that the loops lying in the same area change their shape. This observation was produced because of a geometrical effect. Upon rotation, the projection of the disk contained in a given habit plane onto the plane perpendicular to the electron beam changes, and when the g.b = 0 condition is fulfilled, it makes them invisible. By taking images of each condition and performing a subsequent analysis, it is possible to determine the value of the Burgers vector. It is important to emphasise that the value of the extinction vector, s, was always positive.

This method was widely applied in the investigations of dislocations and dislocation loops. Prokhotsdeva et al. [11] have developed a statistical method that facilitates its calculation. However, it is a laborious but necessary method if the loop is smaller than 10 nm in size. On the other hand, if the loop sizes are significant, it is possible to identify their Burgers vector if one has prior knowledge of the expected Burgers vector and its geometrical projection in the plane perpendicular to the electron beam (microscope viewing plane). The shape will depend on the zone axis under which one is working, as shown in Figure 4. More information on this method was published in [29]. This methodology is valid if most of the loops are large, especially if one wants to determine the swelling produced by them.

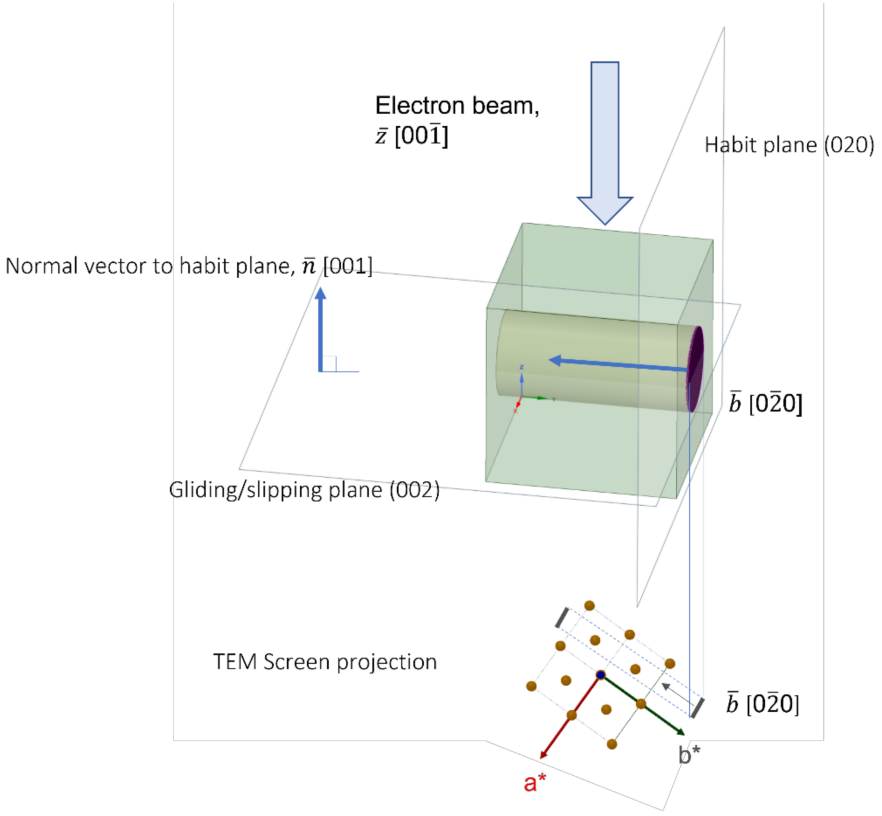


Figure 4. Relationship between the electron beam and the TEM view plane, b, and the loop habit plane. The projection of b depends on the zone axis and the foil orientation.

An example of this series of images with large-sized loops is presented in Figure 5, as these are similar to those found in all samples. Depending on the diffraction conditions, some loops change from visible to invisible. In Figure 5a, the central area of the image represents the fact that the crystal is under zone-axis conditions (high diffraction contrast), in particular under [00$\bar{1}$]. In addition, different g vectors are observed since the two-beam diffraction condition is satisfied in every direction. The bent crystal foils of pseudo-constant thickness as this one show long and curved bend contours. Lines with the same intensity contrast represent equal inclination of the lattice planes to the electron beam. The broadest bands are usually superpositions of low-index reflections with the regions of diffraction contrast overlap. Figure 5b–d show the same area with different g vectors and hence the visible loops are only the ones whose Burger vector is not in parallel to the g vector, meaning b.g $\neq 0$.

After observing that the loops were large and that most of them had their habit plane in {200}, to calculate their average size and population in a relatively easy way, g, a low index <112> near the main zone axes <110> and <111>, was determined to be the best diffraction vector. With this diffraction vector, all three families of the loops with {200} habit planes and 3 of 4 families with {111} habit plane can be observed, therefore this procedure underestimates the relative population of loops since only 75% of the {111} are considered. However, generally speaking, very few of the $\pm\frac{1}{2}a_0$<111>{111} type is observed in each condition, so the results are considered reasonably accurate.

Once the size distribution is determined, assuming that the loops are pure-edge type prismatic and disk-shaped, we determine the family to which each loop belongs. Firstly, this is achieved by discriminating between the two types of habit planes {200} or {111} and then assigning them the correct one. It is necessary to obtain images with different diffraction conditions, considering the fact that the g vector does not belong to both zone axes. They must be linearly independent.

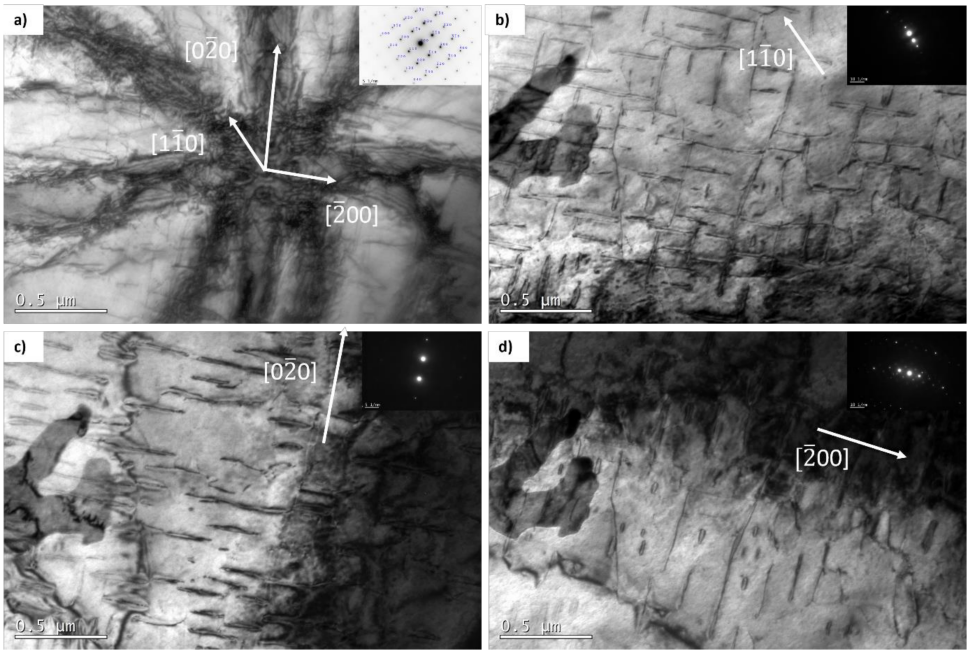


Figure 5. TEM micrographs of pure iron irradiated with 20 MeV at 300 °C and high dose showing (**a**) bend contours under the [00$\bar{1}$] zone axis, and dislocation loops under (**b**) (1$\bar{1}$0), (**c**) (0$\bar{2}$0), and (**d**) ($\bar{2}$00) diffraction vectors.

Since nature studies and the complete designation of b are to be performed, at least 3 zone axes must be chosen. By calculating the tilt between them, a portion of the Kikuchi map can be constructed. An equation that calculates the effective angle between two planes using the values of the double-axis holder tilting can be found in [30]. This way, it is possible to assign the correct signs to the different diffraction vectors using the ±g pair plus the axis of the b method so as not to exceed a crystal twist angle called unsafe [31]. Figure 6 shows a portion of the Kikuchi map between three zone axes. The rotation of each axis of the double-tilt holder was included, and the convergent-beam electron diffraction (CBED) images where the Kikuchi paths and the corresponding diffraction vectors can be seen.

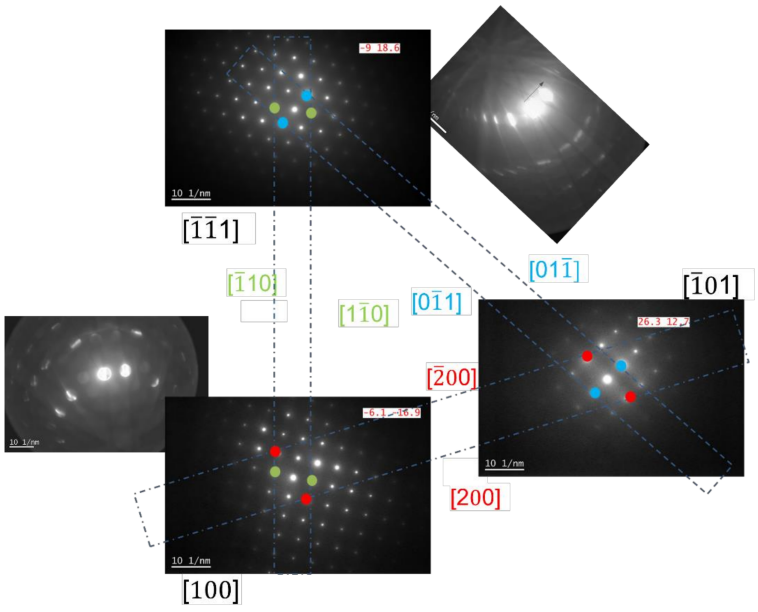


Figure 6. Kikuchi map between 3 zone-axes, including the values of the diffraction vectors.

Once the portion of the Kikuchi map was known, to determine the habit plane of the observed loops, different images were taken in which the diffraction conditions were two-beam, with a positive extinction parameter (s > 0). Suppose that the loops are larger than 5 nm. In that case, it is possible to make a morphological comparison by constructing a BCC structure with lattice parameter 2.86 Å, which would be oriented as a function of the zone axis under which the observations were made. Knowing that the b-vectors of the loops would be $\pm a_0$<100> or $\pm\frac{1}{2}a_0$<111> as well as their habit planes {200} and {111} respectively, it was possible to identify in most cases to which family they belonged. In addition, sometimes this was possible for one in particular (assuming the equivalents $\pm$ as a type) by a morphological comparison, without the need to perform more complex analyses such as the one proposed in [11] for small size loops, of the embryo type, where a morphological comparison is unfeasible.

Traditionally, methods quantify their density as a function of the volume corresponding to each micrograph analysed to characterise materials that present dislocations. However, suppose it is desired to estimate the effect of dislocations on the possible hardening or degradation of mechanical properties. In that case, it is estimated that an evaluation of the ratio of the volume that the loops modified because of their nucleation and growth is more relevant as well as clarifying since the mentioned ratio corresponds to the swelling produced by dis-location loops, which traditionally has been related only to cavities.

Finally, the value of swelling that the thin film has undergone by irradiation will be calculated. For this, it was necessary to distinguish the nature of the loops since an interstitial loop will add atoms to the defined control volume, and a vacancy loop will eliminate them. The chosen method to reveal their nature was the well-known inside/outside contrast [32]. On the other hand, the loops will be defined as disks with a height corresponding to the value of the b modulus, which is positive for interstitial loop and negative for vacancy ones. The depth of every micrograph was determined using a CBED pattern, as shown as example in Figure 7, and the distance between the parallel Kossel–Möllenstedt fringes [33].

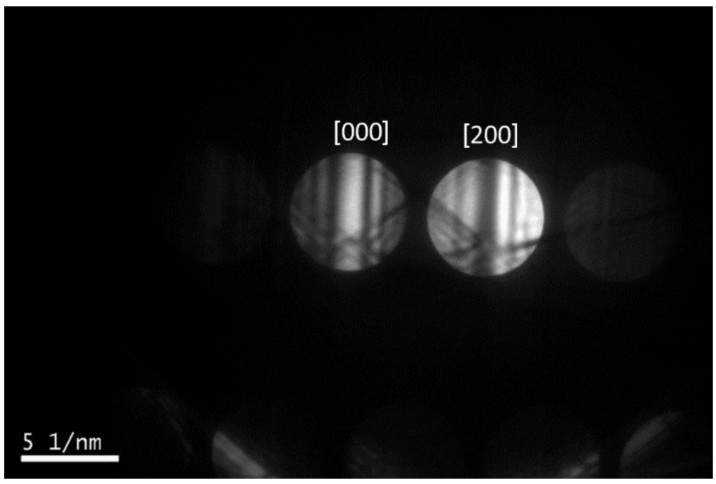


Figure 7. CBED pattern to calculate the thickness of the sample at a certain point.

3. Results

3.1. Simulation

The primary knock-on atom (PKA) spectrum of the bulk experiment and thin film using MARLOWE [34,35] was calculated to evaluate whether both experiments are comparable regarding energy deposition. As observed in Figure 8, both curves are practically the same but slightly different at low probability. This result means that the most significant probability of PKA is for energies lower than 10 eV, which is very low and makes both experiments comparable in terms of energy deposition.

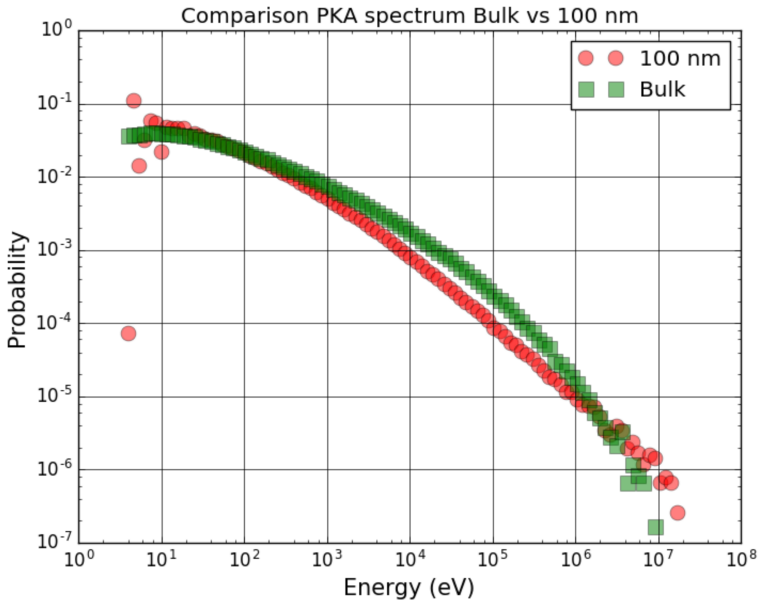


Figure 8. PKA spectrum comparing thin films (100 nm) and bulk by means of MARLOWE code.

3.2. Bulk Specimens

The entire irradiation depth was contained within the lamella extracted from the specimens for bulk studies, as shown in Figure 9. However, only the first 100–150 nm were considered in this research, so that it could be compared with the thin-film specimens, whose thickness was smaller than 100 nm.

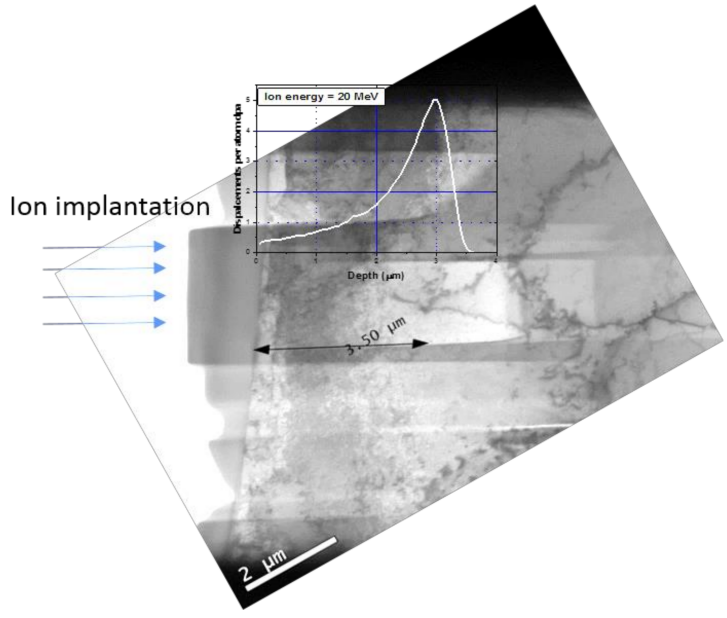


Figure 9. TEM micrograph of the lamella extracted from the sample of EFDA pure Fe irradiated at 300 °C and high dose, showing the irradiated peak wholly contained in the sample.

In all four cases, the defects observed were similar. Tiny black dots (supposedly loop-embryos) but no loops were found, even at high-resolution magnifications, as shown in Figure 10a–c.

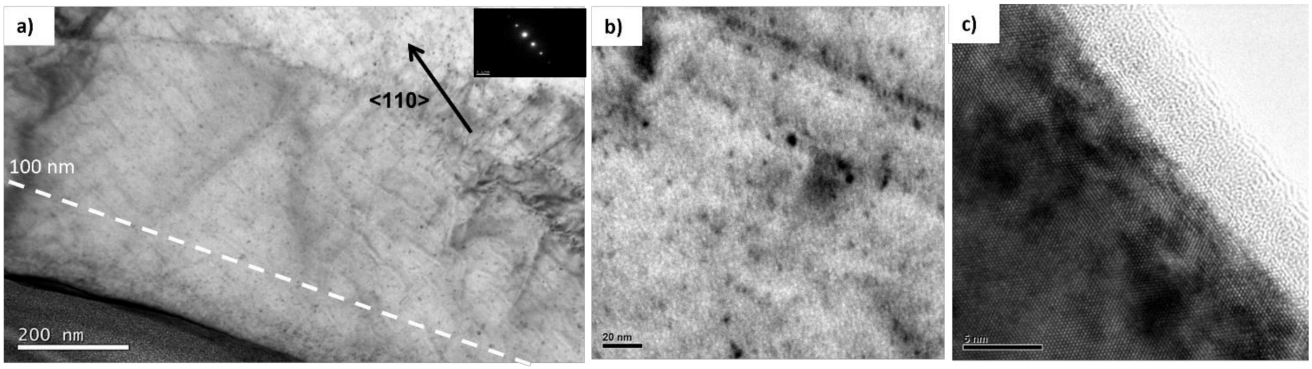


Figure 10. Representative microstructures of the irradiated bulk samples under the same conditions as the thin films, at different magnifications, showing the first 500 nm in depth (**a**), focusing on the first 100 nm (**b**) and very close to the surface (**c**).

However, some cavities were detected at the peak, as observed in Figure 11, along with other defects such as small dislocation loops. However, in summary, no apparent defect generation is observed in the first 100–150 nm of the bulk samples.

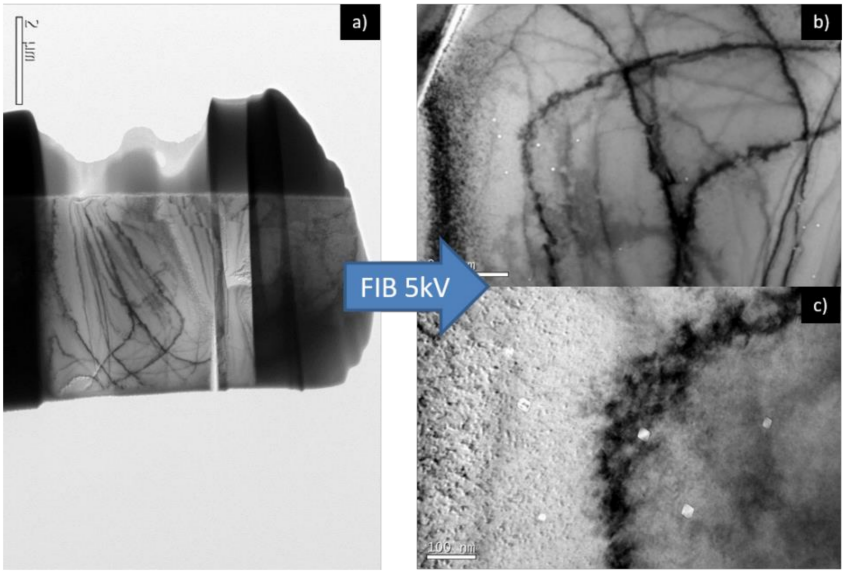


Figure 11. (**a**) Lamella overview irradiated at 300 °C up to 4.27 × 10^{15} cm^{-2}; and (**b**,**c**) cavities observed in the same sample.

It was previously shown that the energy deposition in terms of PKA probability comparing both thin-films and bulk specimens was practically the same. Thus, the next step was to analyse the possible defects generated in the first 150 nm of the bulk specimens. However, as observed in other lamellae extracted from irradiated samples, the Ga ion may produce artifacts. As a result of this, it was decided to electropolish an irradiated disc covering the irradiated surface with a protective commercial lacker (Lacomit) to precisely place the electropolished hole at the irradiated surface.

In Figure 12, a scheme of the process is depicted, and it was performed as follows. To start with, a 3 mm disc was irradiated with Fe ions at 20 MeV producing a shallow layer of 3 μm of damage. Then, when the depth of interest was close to the very surface of the disc, a very thin, homogenous layer of varnish was spread over the surface, protecting it from the electropolishing process. As a result, the hole was successfully created at the surface, as observed in the mentioned figure. The irradiation damage calculated from the

SRIM simulation on the left close to the surface practically corresponds with the damage obtained in the thin films.

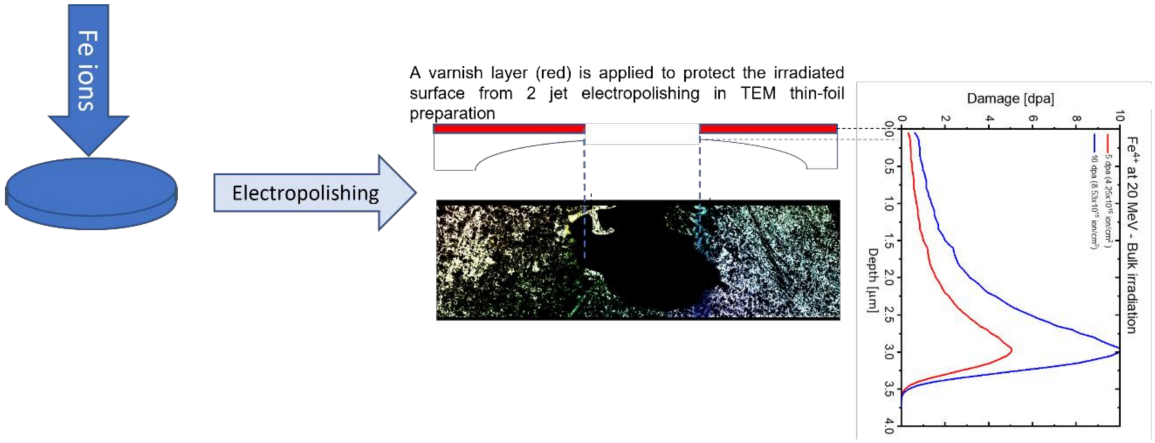


Figure 12. Scheme of electropolished irradiated specimen protected with a varnish.

An in-depth TEM study was conducted afterward on the four irradiated discs specimens previously analysed in the form of thin films (300 and 450 °C irradiated at high and low doses, Figure 13a,b). In all cases, the hole was placed at or very close to the very surface, thus, generally speaking, the comparison is possible. Regarding defects, none of them showed loops (not even the small ones as found on irradiated thin films). Only in the case of 450 °C and high-dose Figure 13b could small black dots (maybe embryo-like loops) be observed (highlighted with red ovals). In summary, the size and type of defects are mostly similar between the FIBed and electropolished samples. There are no large loops, and their distribution turned out to be very heterogeneous.

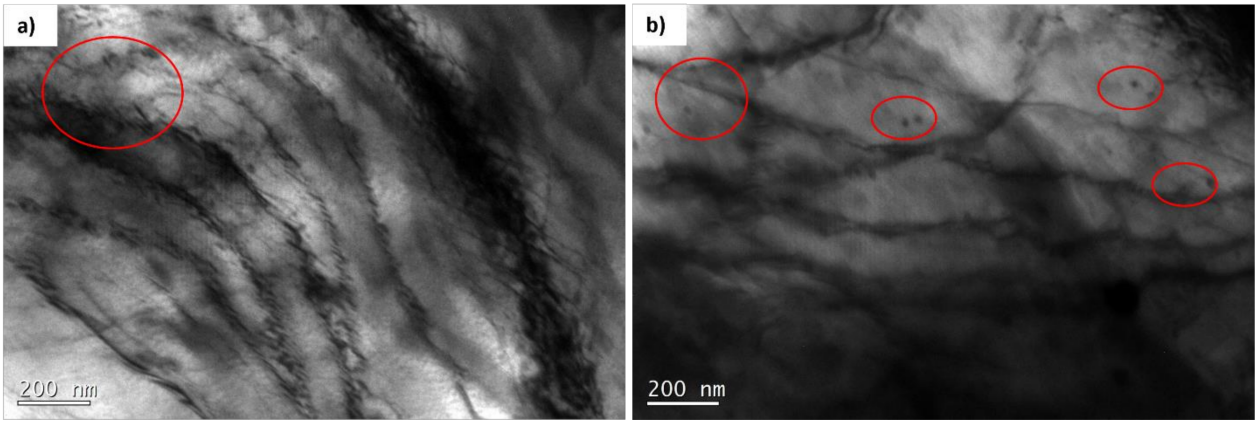


Figure 13. TEM micrograph of electropolished discs protecting the irradiated surface with a varnish irradiated (**a**) at 300 °C and low dose and (**b**) at 450 °C and high dose. Some of the defects detected in the microstructure are highlighted with red ovals.

3.3. Thin-Film Specimens

3.3.1. Loop Size Distribution

A minimum count of 300 loops was established due to the loop size to have relatively good statistics. As a limit, those whose diameters were more significant than or equal to 10 nm were counted; since the analysis area was large, such small loops were not correctly resolved and could be misleading. Figure 14 shows the histograms obtained from the measurements as a function of the relative frequency, and Figure 15 shows the mean size and its standard deviation.

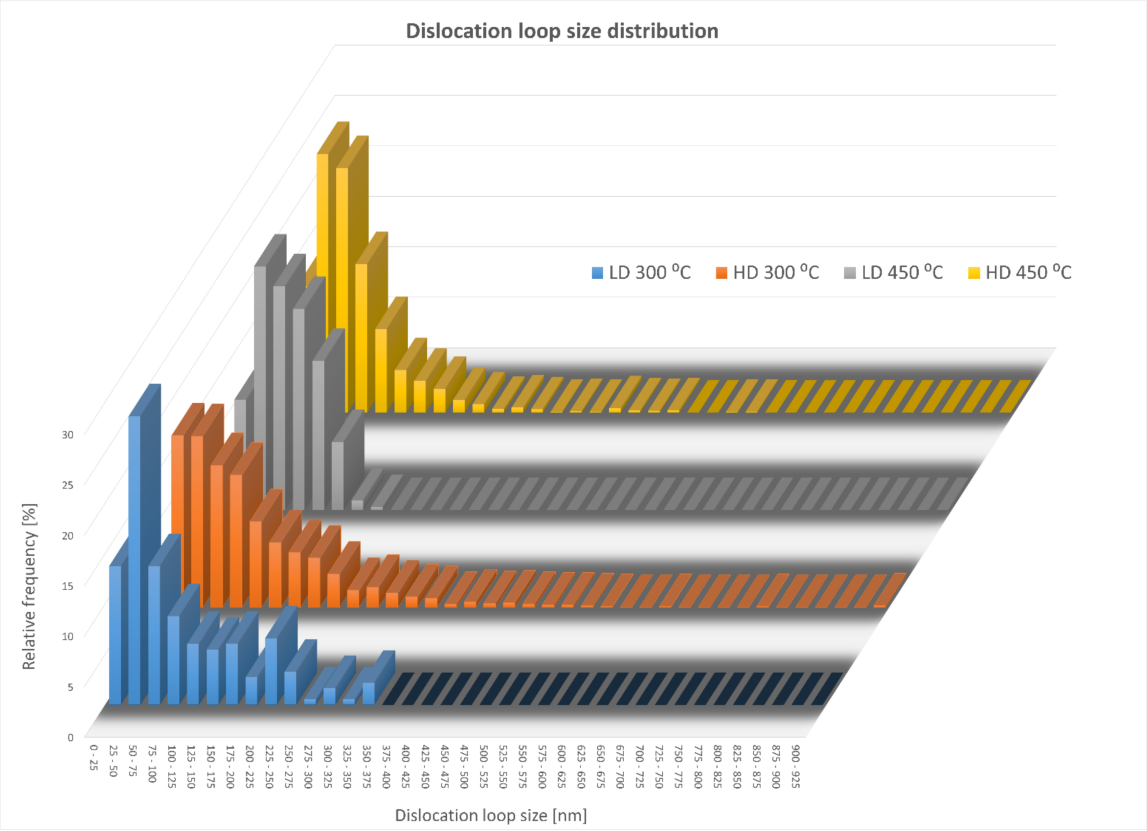


Figure 14. Distribution of dislocation loop sizes under the g vector (112) for an Fe thin foil irradiated with 20 MeV at (**a**) 300 °C, 4.25 × 10^{15} ions/cm^2; (**b**) 300 °C, 8.5 × 10^{15} ions/cm^2; (**c**) 450 °C, 4.25 × 10^{15} ions/cm^2; and (**d**) 450 °C, 8.5 × 10^{15} ions/cm^2.

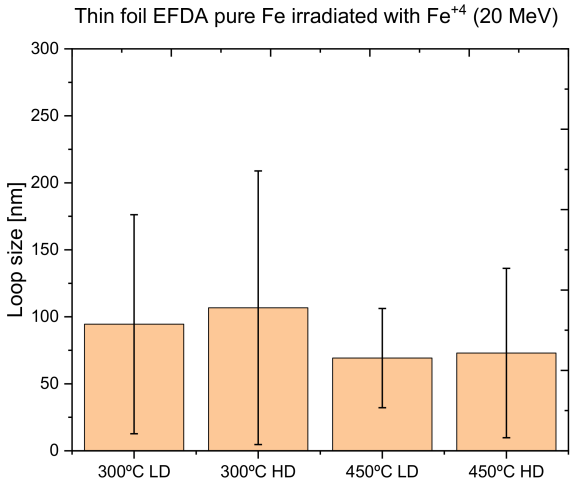


Figure 15. Loop mean size and standard deviation for all the irradiation conditions.

Both representations analysed together perfectly describe the loop size distribution and their heterogeneity as a function of the experimental conditions. It can be observed that increasing the dose while maintaining the temperature at 300 °C generates the growth of loops, as shown in Figure 16, which contains the largest loop detected in the four experimental conditions of ~1 µm. In other words, growth is enhanced as opposed to the generation of new defects. On the other hand, such a dose increase at high temperature also produces this effect, but to a much milder extent. Thus, it seems that the formation of medium-sized loops (of approximately 50–100 nm) prevails overgrowth for the actual

experimental condition. In addition, this micrograph represents a phenomenon that must be considered when studying thin foils with a slight bend; the loops with a much more intense contrast satisfy that b.g = 1, for g [200]. However, another weaker reflection is excited, g [3$\bar{1}$2], revealing the loop arrangement highlighted in the blue oval. This quasi-mixed diffraction condition shows that there may be a greater interconnection between loops than would appear if only g [200] had been excited. On the other hand, within the red circles, $\pm\frac{1}{2}a_0$<111> loops are shown, which, despite appearing small, are approximately 20–30 nm in size.

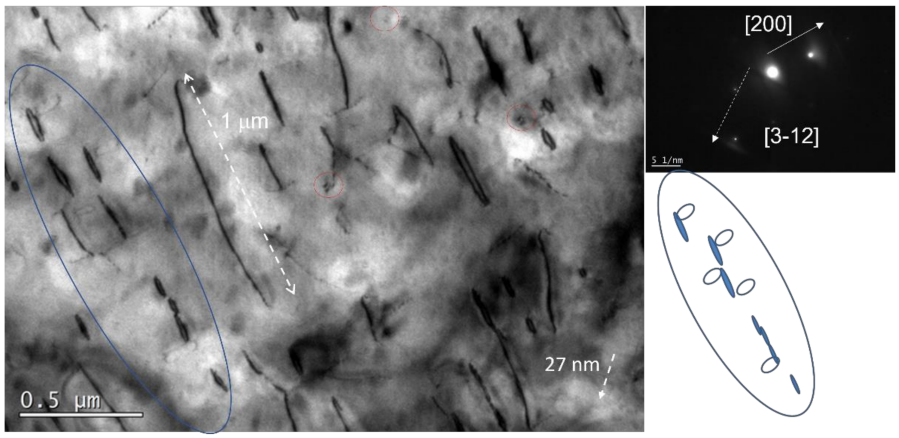


Figure 16. TEM micrograph from the Fe sample irradiated at HD and 300 °C with Fe^{+4} at 20 MeV.

In all the samples, some zones are irregular in thickness. It is possible that it slightly alters the measurements because when the crystal had slight bending, the dynamic diffraction condition (slightly away from the zone of higher contrast) no longer met in a few nm. Thus, the volume of material analysed was relatively smaller than samples whose thickness was kept more constant. Figure 17 shows representative micrographs of the loops found under the conditions discussed above (g <112>, under {111}, with s > 0). The images that best describe the global set of defects found were selected.

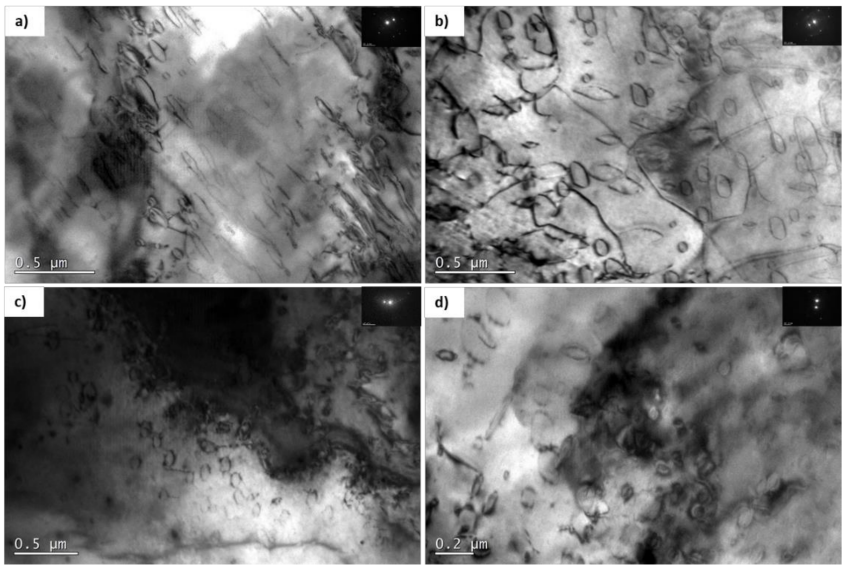


Figure 17. Representative TEM microstructures of the distribution of dislocation loops observed under g vector <112> near {111} zone axis, irradiated with 20 MeV at (**a**) 300 °C, 4.25 × 10^{15} ions/cm^2; (**b**) 300 °C, 8.5 × 10^{15} ions/cm^2; (**c**) 450 °C, 4.25 × 10^{15} ions/cm^2; and (**d**) 450 °C, 8.5 × 10^{15} ions/cm^2.

3.3.2. Loop Habit Plane

In the following, the observed microstructure of each experimental condition will be described after analysing the different zones of each sample together. This way, the random choice of any zone, which may be uncharacteristic of the whole sample, is minimised. Studies were carried out in different transparent zones of the irradiated disk, under three different zone axes, trying to find areas as homogeneous as possible in terms of thickness and linear dislocations. However, in some zones, there were dislocations which possibly affected the evolution of the loops.

On the right side of each micrograph, one can see how the unit cell is oriented and the projections of the different types of visible loops lie on their respective habit plane. The atomic representations are built with respect to the angle formed between the zone axis and a plane (002) perpendicular to the electron beam (which symbolises the phosphoric screen). Thus, it is possible to see how the morphology of the loops in the micrographs matches entirely with the schemes, except for the smallest loops with no oval shape.

Low Dose (4.25×10^{15} ion/cm^2) at 300 °C

Only considering loops of size equal to or larger than 10 nm, the pure iron EFDA sample irradiated at 300 °C with Fe ions at 20 MeV up to a dose of 4.25×10^{15} ions/cm^2 shows that 92% of the detected and characterised loop population belonged to the family of loops with a Burger vector of family $\pm a_0$<100> whose habit planes were of family {200}. Specifically, after analysing the different zones of the sample, under three different zone axes, almost 60% were ±a0[001](002), 27% ±a0[010](020), and the rest, approximately 8% ±a0[100](200). In Figure 18a, the overall result of the observations is very clearly reflected. Under dynamic two-beam conditions (s > 0) under the zone axis [1$\bar{1}$1] and with a diffraction vector g [132], all loops of the $\pm a_0$<100> family should be visible since they all satisfy that b.g $\neq 0$ and b.g> |1|. However, the vast majority were ±a0[001](002). If only the observations in Figure 18b were taken into account, under axis [$\bar{1}$10] and g [002], one could reach the same conclusion; however, erroneously, since with these conditions, the loops ±a0[010](020) and ±a0[100](200) are invisible.

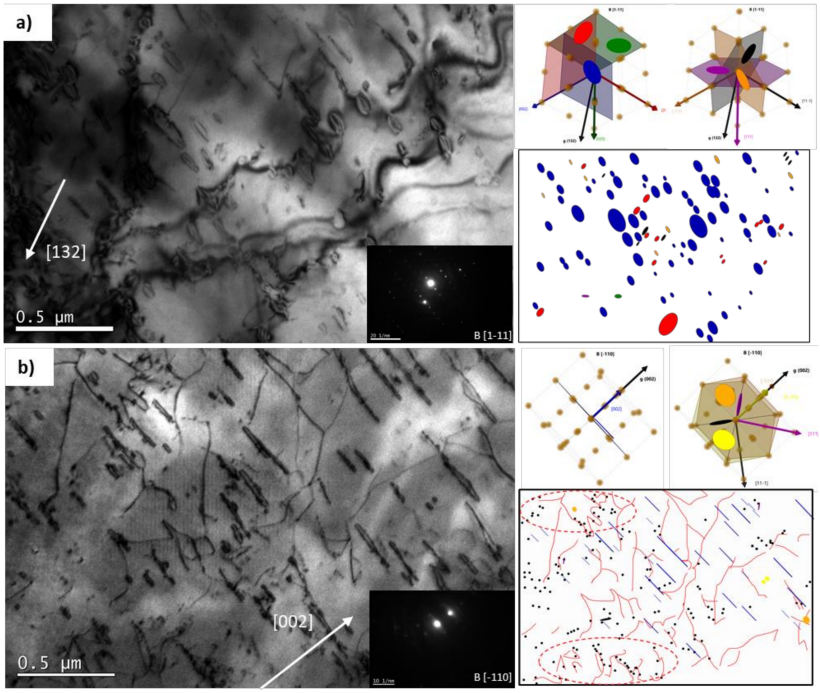


Figure 18. TEM micrographs of EFDA pure-iron thin film irradiated with 20 MeV at 300 °C up to 4.25×10^{15} ions/cm^2 near the [1$\bar{1}$1] and [$\bar{1}$10] zone axis with two beam diffraction contrast condition along (**a**) [132] and (**b**) [002].

On the other hand, 8% of the total number of observed and uniquely identified defects had a b $\pm\frac{1}{2}a_0$<111> family in {111} habit planes. However, there were no loops with a predominant Burgers vector, unlike the $\pm a_0$<100> loops which exhibited this very clearly.

Although sizes of a minimum of 10 to almost 200 nm were detected, the average value was 95 ± 80 nm, and the maximum size detected was 348 nm. The largest, in general terms, was the most frequent loops ±a0[001](002). Small clusters, heterogeneously distributed in the matrix, such as those highlighted with a red circle in Figure 18b, were observed in all the analysed areas. Although it was impossible to assign them a habit plane with this method in most cases, they seemed to present a contrast that could possibly resemble $\pm\frac{1}{2}a_0$<111>. On the other hand, a phenomenon that did recur in different samples for containing linear dislocations was the accumulation of these small-sized loops around them, as shown in the graphical representation in Figure 18b, where the red lines represent the dislocations and the black dots, possible uncharacterised loops (embryos). The observations seem to indicate that they were trapped during their movement, since in the areas where there are no linear dislocations, the population density of the loops increases. Larger loops were also observed, although this was not the most common.

High Dose (8.5×10^{15} ion/cm^2) at 300 °C

The pure iron EFDA sample irradiated at 300 °C with Fe ions at 20 MeV up to a dose of 8.5×10^{15} ions/cm^2 shows a population of dislocation loops similar to the sample irradiated at a low dose and at the same temperature. Approximately 80% of all the loops analysed in this sample present a Burgers vector of the $\pm a_0$<100> family with the {200} habit plane. Although there is a reduction in the population of loops with b of this family, it was determined that, after increasing the dose, loops with the largest size of the four conditions studied are identified, and the largest of all is 907 nm. The size is 110 ± 100 nm, reflecting the high range of sizes present in this sample.

Regarding the loops with the Burgers vector $\pm\frac{1}{2}a_0$<111>, it was observed that they have increased both in size and population, almost 20% of the total. Although in relative terms, this remains low compared to the presence and size of the $\pm a_0$<100>, it is a relevant population. Of the four families of loops $\pm\frac{1}{2}a_0$<111> (without discriminating by direction), the $\pm\frac{1}{2}a_0[1\bar{1}1](1\bar{1}1)$ and $\pm\frac{1}{2}a_0[\bar{1}11](\bar{1}11)$ are the most frequent with almost 7% of the total number of loops identified.

In the sample irradiated under these experimental conditions, it was not determined that there was one Burgers vector/preferential habit plane, but rather two. The largest population corresponds to ±a0[010](020) with slightly more than 37%, but is closely followed with 32% by ±a0[100](200), the smallest population with almost 11% by ±a0[001](002). It is striking that the majority population in the case of irradiation at 300 °C and LD is under these conditions the least detected, dropping from almost 60% to 11%. This is probably not due to an effect of the increased dose per se, but in addition to increased radiation damage, this sample must have microstructural features that so clearly intervene in the evolution of defects. This may be due to the orientation of the grain to the beam and those of its free surfaces.

Figure 19 shows three micrographs obtained under different diffraction conditions under three different zone axes: (a) [0$\bar{1}$2], g [$\bar{1}2\bar{1}$]; (b) [$\bar{1}1\bar{3}$], g [$\bar{1}2\bar{1}$]; and (c) [111], g [$\bar{2}11$]. In all of them, the loops ±a0<100> fulfil the following: b.g $\neq 0$ and b.g> |1|—whilst it was observed that the population of ±a0[001](002) loops was the smallest, qualitatively appreciating how the density of ±a0[100](200) and ±a0[010](020) loops are similar.

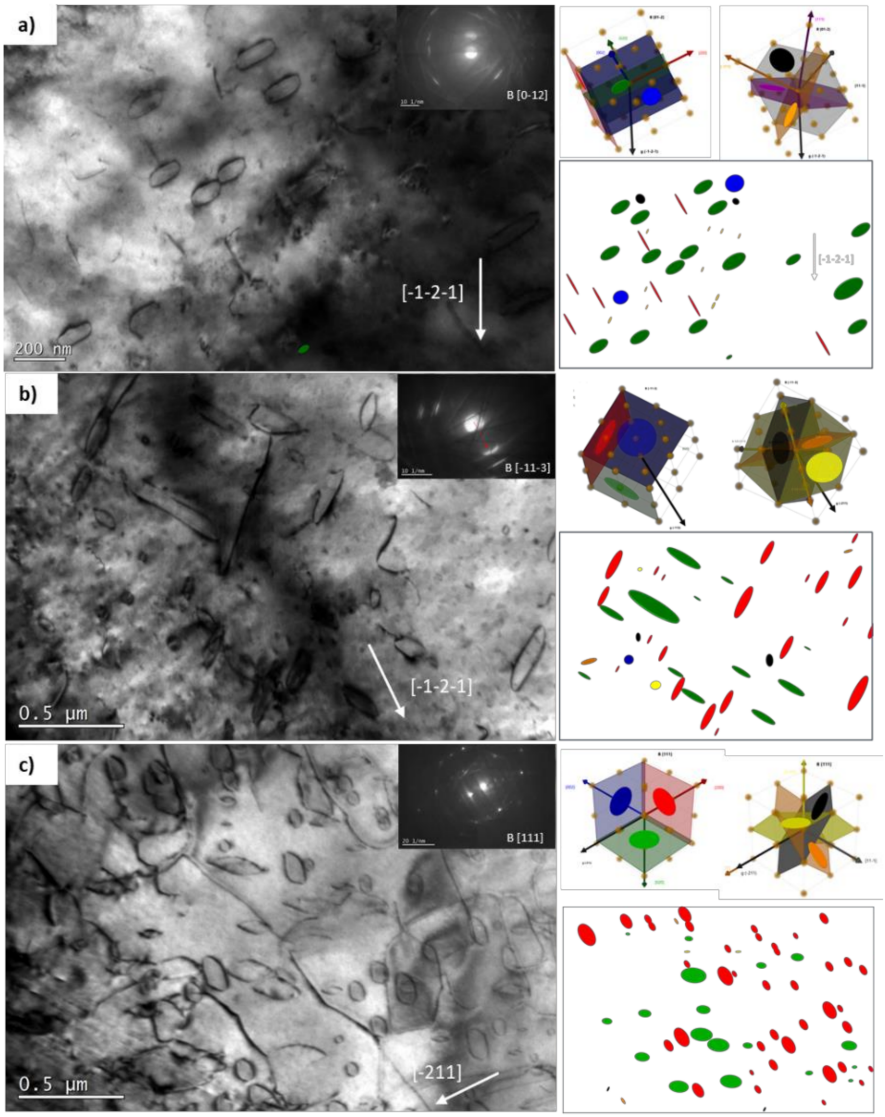


Figure 19. TEM micrographs of pure EFDA iron irradiated with Fe ions at 20 MeV at 300 °C up to 8.5 × 10^{15} ions/cm^2 under (**a**) [0$\bar{1}$2] with g [$\bar{1}\bar{2}\bar{1}$]; (**b**) [$\bar{1}$1$\bar{3}$] with g [$\bar{1}\bar{2}\bar{1}$]; and (**c**) [111] with g [$\bar{2}$11], showing the results for every area.

Low Dose (4.25 × 10^{15} ion/cm^2) at 450 °C

In the pure iron EFDA sample irradiated at 450 °C with Fe ions at 20 MeV up to a dose of 4.25 × 10^{15} ions/cm^2, 85% of all identified loops are of the ±a$_0$<100> family with the {200} habit plane.

The average size is 70 ± 40 nm, the smallest and most homogeneous of the four samples studied. Regarding the loops with a Burgers vector $\pm\frac{1}{2}$a$_0$<111>, the predominant family with 55.5% of the population concerning the total of $\pm\frac{1}{2}$a$_0$<111> detected was the $\pm\frac{1}{2}$a0[11$\bar{1}$](11$\bar{1}$).

Figure 20 shows three micrographs obtained under different diffraction conditions under two different zone axes. Figure 20a under [10$\bar{1}$] with g [0$\bar{2}$0] shows ±a0[010](020) loops in green completely perpendicular to the diffraction vector. Furthermore, with these diffraction conditions, all loops $\pm\frac{1}{2}$a0<111> should be visible, because with g {200}, they all fulfil b.g > |1|; however, only four loops b $\pm\frac{1}{2}$a$_0$<111> were identified which could be $\pm\frac{1}{2}$a$_0$[$\bar{1}$11]($\bar{1}$11) or $\pm\frac{1}{2}$a$_0$[11$\bar{1}$](11$\bar{1}$). Figure 20b,c are taken under the same zone axis [$\bar{1}\bar{1}\bar{1}$] with different diffraction vectors, g [01$\bar{1}$] and g [$\bar{2}$11], respectively. The respective microstructures very clearly describe an observation that was present in the whole sample.

In no area of the studied crystal were ±a0[100](200), ±a0[010](020), and ±a0[001](002) loops with a similar population density detected. A similar number of loops with b ±a0[010](020) and ±a0[001](002) together (b) or ±a0[100](200) were dominant (c), which was the least frequent microstructural distribution.

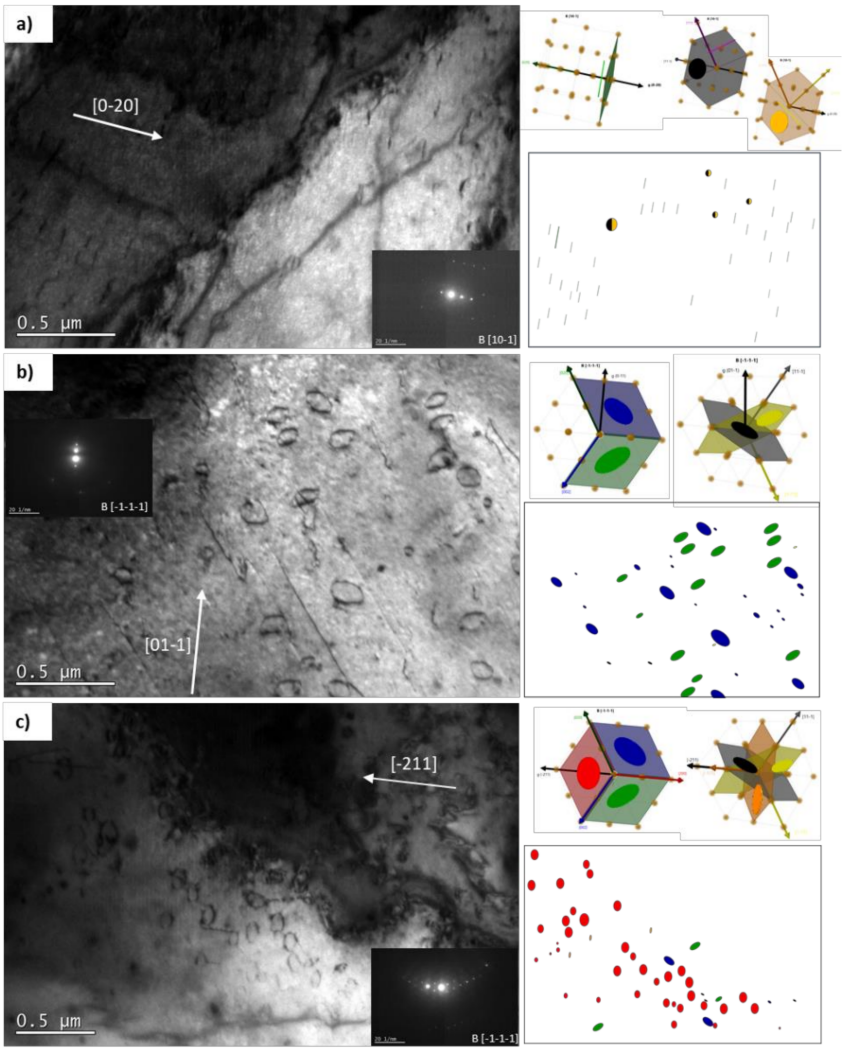


Figure 20. TEM micrographs of pure EFDA iron irradiated with Fe ions at 20 MeV at 300 °C up to 8.5×10^{15} ions/cm^2 under (**a**) [10$\bar{1}$] with g [0$\bar{2}$0]; (**b**) [$\bar{1}\bar{1}\bar{1}$] with g [01$\bar{1}$]; and (**c**) [$\bar{1}\bar{1}\bar{1}$] with g [$\bar{2}$11], showing the results for every area.

High Dose (8.5×10^{15} ion/cm^2) at 450 °C

The sample irradiated up to a dose of 8.5×10^{15} ions/cm^2 at 450 °C contained 92% of loops with a Burgers vector of the ±a_0<100> family with {200} habit planes. As for the distribution of loops according to b, it was the sample with the most homogeneous distribution. It was calculated that 38% of the loops were ±a0[100](200), 27.5% ±a0[010](020) and 26% ±a0[001](002). The average loop size was 75 ± 60 nm, with the maximum loop size being 577 nm.

Figure 21 shows three micrographs obtained under different diffraction conditions under three different zone axes: (a) [111], g [1$\bar{1}$0]; (b) [131], g [$\bar{1}$01]; and (c) [$\bar{1}\bar{1}\bar{1}$], g [112]. Figure 21a,b show 2/3 type ±a_0<100> and 2/4 type ±$\frac{1}{2}a_0$<111> loops so that it can be seen that there is no family of type ±a_0<100> loops that predominates over the others. However, probably due to the randomness of the processes or to the effect of some variables such as sample thickness, surface orientation, etc., in global terms, it seems that the ±a0[100](200) loops are the most frequent. In addition, in these figures, the existence of the so-called open

loops can be observed, i.e., loops anchored to the surface whose extra interstitial plane is cut. This sample is the one that shows more defects of this type, and although there is no convincing explanation, everything seems to indicate the fact that the high temperature and smaller thickness of the sample enhanced the formation of these open loops.

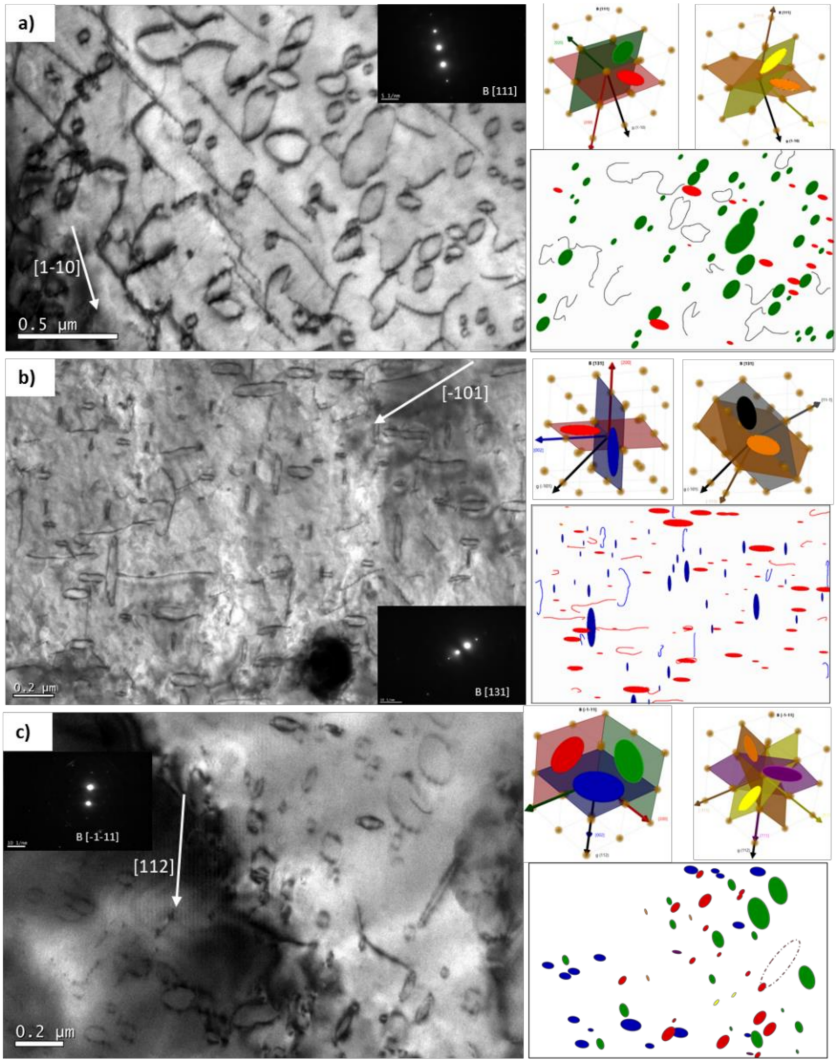


Figure 21. TEM micrographs of pure EFDA iron irradiated with Fe ions at 20 MeV at 300 °C up to 8.5×10^{15} ions/cm^2 under (**a**) [111] with g [$1\bar{1}0$]; (**b**) [131] with g [$\bar{1}01$]; and (**c**) [$\bar{1}\bar{1}1$] with g [112] showing the results for every area.

Figure 21c, finally, represents an overall picture of the coexistence of the three families of loops $\pm a_0$<100> together with some $\pm\frac{1}{2}a_0$<111> of small size. Thus, for example, the habit plane of a loop highlighted in a red dotted oval appears to be ($1\bar{1}1$), but its angle ratio (angle between the zone axis vector, B, and b, related to the projection between the diagonals of the oval) does not coincide with a projection of a loop with b $\pm\frac{1}{2}a_0[1\bar{1}1]$.

Analysis of the Results

Comparing the four samples, it is evident that the population of loops located in the {200} planes result in the great majority of the loops observed, although an increase in the {111} type was observed for the sample irradiated at high dose and low temperature, Figure 22. Usually, with a diffraction vector that allows the {200} loops to be visible, such as the <112> direction, all three types should be observed, but here this is not the case; if

this does occur, then the population of one of them is almost irrelevant compared to the number of defects of the other two (Figure 21a).

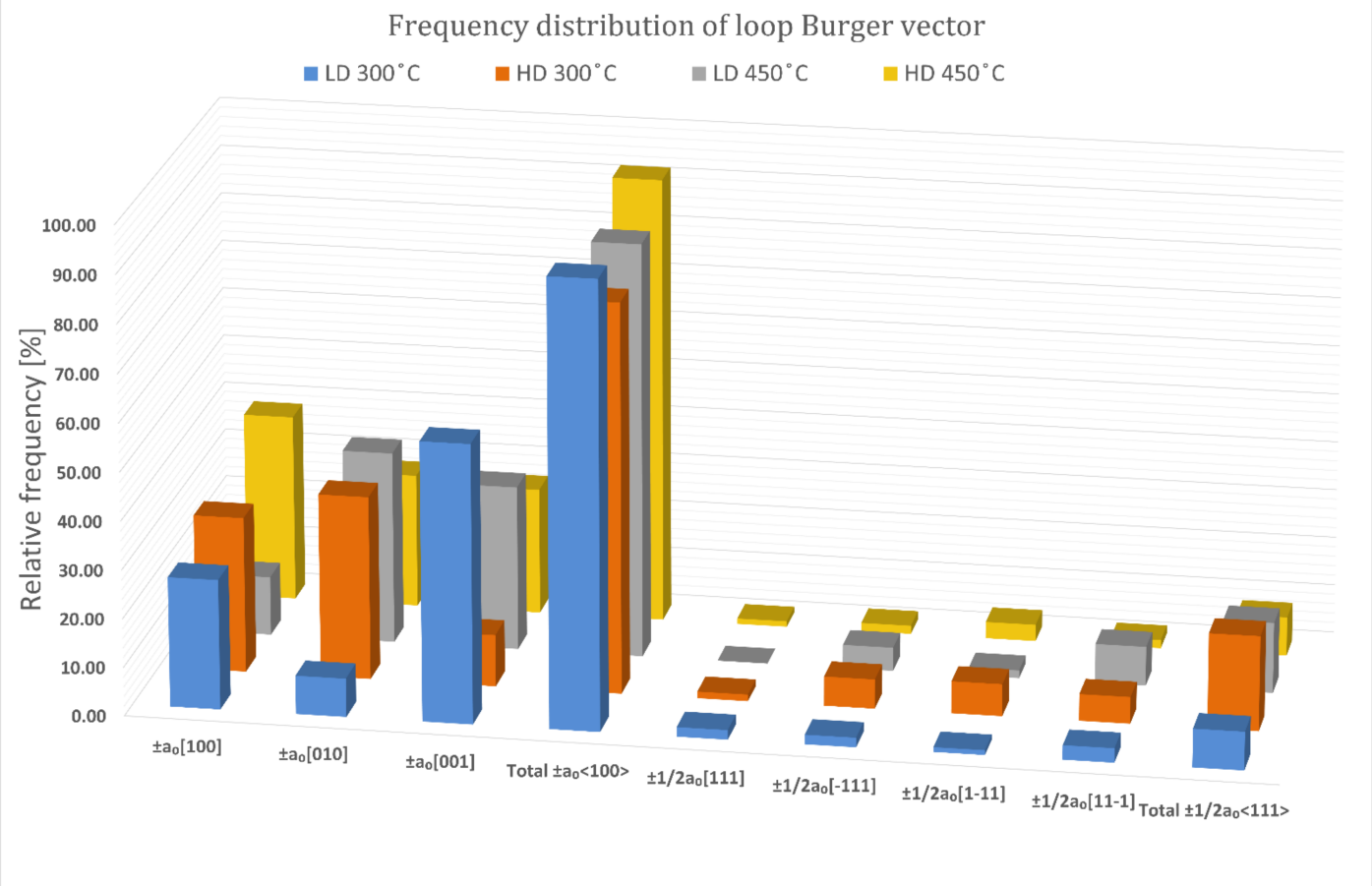


Figure 22. Frequency distribution of Burger vector of the dislocation loops observed in all specimens.

3.3.3. Swelling

A study of the volume variation due to the generation of dislocation loops and voids was performed. As described in the experimental development section, to accurately perform these calculations, it is necessary to determine the particular Burger vector (not just the habit plane) and subsequently apply the inside–outside (I-O) method to determine the nature of each loop individually. During the process of establishing the crystal map through the Kikuchi paths using three zone axes, sometimes the contrast of the area significantly varied. Moreover, because of the ferromagnetism of the disk concerning the polar lens, the image was not good or there could even be a high drift—or in the worst case, the sample jumped, losing the references of the successive turns of the double sample holder. Despite these reasons, approximately 250 loops were analysed, especially with the diffraction vectors g of type <122> so that the $\pm a_0$<100> loops and the relative averages for the calculation of the total of type $\pm\frac{1}{2}a_0$<111> were visible.

Figure 23 shows some examples of the areas analysed using the I-O method for all the conditions studied. In addition to representing the contrast change so evident in large loops, it is essential to know how to interpret the contrast limit s > 0 of the micrograph and not to analyse loops that are already being excited with other diffraction conditions and that may show a different contrast change. On the other hand, it is necessary to establish the maximum sample rotation, where the I-O contrast change remains constant, which is called the "safe zone", since, beyond that angle, the direction of the change is reversed and can lead, again, to misinterpretations.

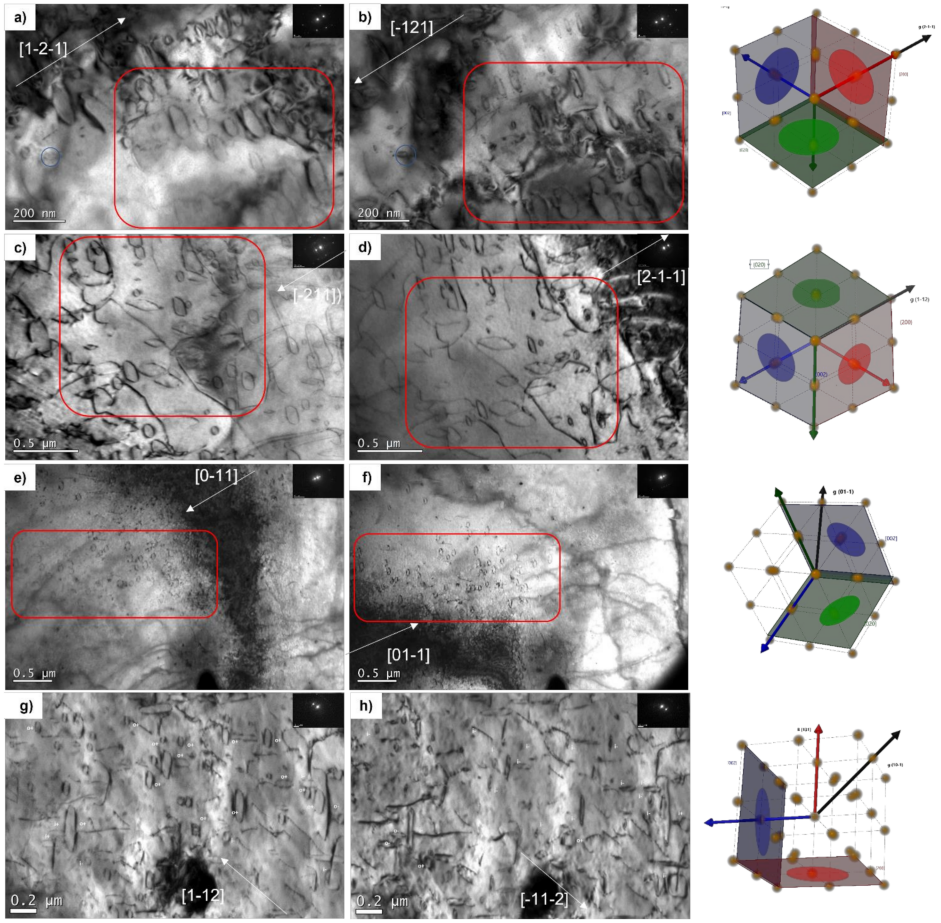


Figure 23. Inside–outside method to study the nature of the visible loops at (**a**,**b**) low dose and 300 °C; (**c**,**d**) low dose 450 °C; (**e**,**f**) high dose 300 °C; and (**g**,**h**) high dose and 450 °C.

Figure 23a–h shows different micrographs where the I-O method was applied. Figure 23a,b belongs to the sample irradiated at 300 ^{O}C up to a dose of 4.25 × 10^{15} ion/cm^2. The diffraction vector was in (a) $(1\bar{2}\bar{1})$ and in (b) $(\bar{1}21)$, which results in b.g$_a$ < 0 and b.g$_b$ > 0. Therefore, to meet this criterion, the observed loops located in the habit plane (020) must have an "inside" type contrast at a, and vice versa. It is observed that the contrast of the most prominent loops is, on the contrary, "outside" in Figure 23 and "inside" in b, therefore, the plane is $(0\bar{2}0)$. It was determined that if the size of the loop decreases when changing from the outside to inside contrast, it is of interstitial type, which was confirmed. Similar analyses were performed for the other loops and nearby zones under the same zone axis $[\bar{1}\bar{1}1]$. In total, 90% of the analysed loops were interstitials, 5% were vacancies (4% at 300 °C and 1% at 450 °C). The rest could not be confirmed with certainty.

The interpretation of the contrast change to identify the loop nature of Figure 23c,d for LD—450 °C; e and f for HD—300 °C; and g and h for HD—450 °C follows the same procedure as mentioned above. Finally, it can be concluded that the vast majority of the analysed loops were of interstitial type, indicating an increase in volume due to the incorporation of the atomic planes as the loops generated by ion irradiation.

Approximating the micrograph area that maintains the correct diffraction conditions, i.e., the loops being analysed must be revealed by a single diffraction condition, or at least not show a significant change in their contrast or size. Then, the loop-induced swelling and dislocation density were calculated, approximating each loop to a cylinder of height, b, and assuming all as interstitials (Figure 24).

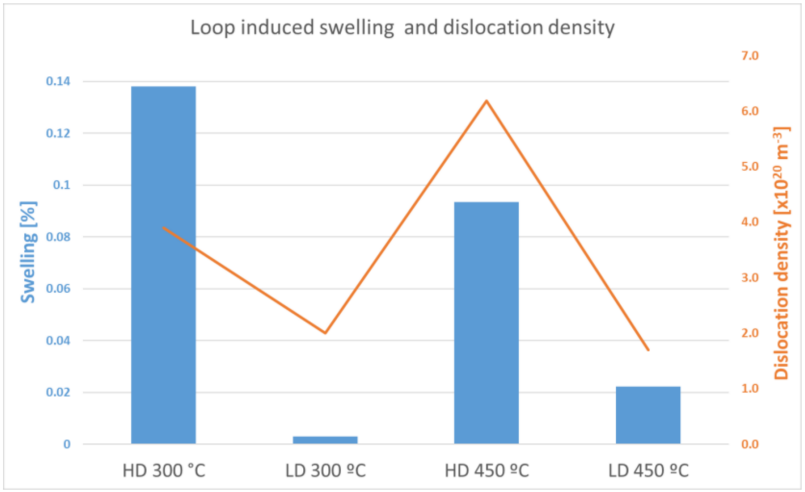


Figure 24. Dislocation-induced swelling and density.

It is important to emphasise that although all samples have a relatively heterogeneous population of defects, the samples with the lowest swelling, which correspond to those that have received a lower dose, have large defect-free areas so the population density decreases in absolute terms (Figure 25).

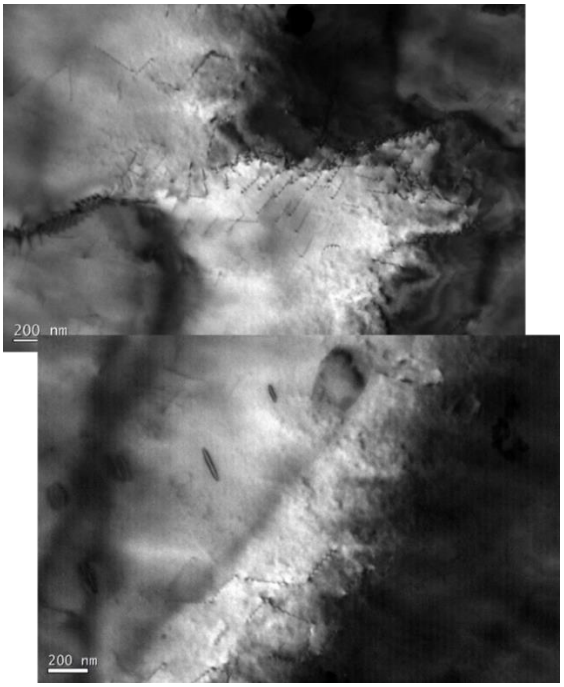


Figure 25. TEM micrograph of the sample irradiated at a low dose and 450 °C showing a large area with a very few dislocation loops and lineal dislocations.

3.3.4. Additional Observation

Effect of Film Thickness

Inherently to thin-film irradiation experiments, a sample thickness increasing effect is expected. Depending on the quality of the electropolishing, the slope will be more or less pronounced to affect the dislocation formation and evolution. For example, in Figure 26, a large transparent area is observed with a high population of large $\pm a_0$<100> loops. However, close to the hole where the sample thickness is lower, almost no loops are observed, even to the left of the dark zone, representing the dynamically excited area, where the contrast condition should also be excited. Then, as the thickness increases, the

population of loops increases. Where the thickness is excessively large, the observation of loops becomes more difficult. On the other hand, the loops' accommodation changes a bit, becoming wider as thickness increases. As a result of this observation, the perfect thickness to perform irradiated thin-film studies was approximately 100 nm because the thinnest samples diminish the diffraction contrast, making it very difficult to obtain, for example, clear two-beam conditions.

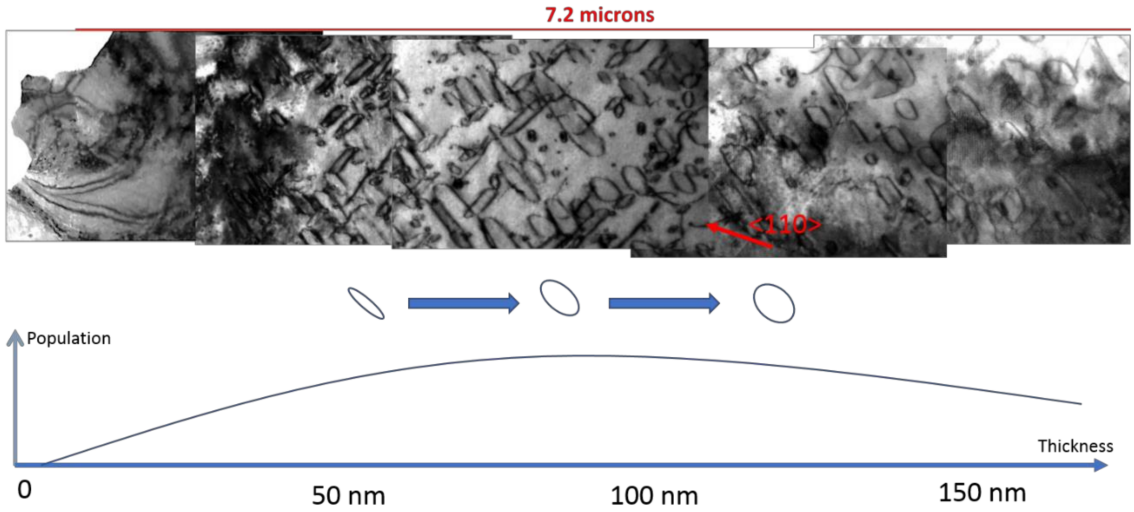


Figure 26. TEM micrograph of irradiated thin film showing the thickness dependence of loops in terms of population and visibility.

Open Loops

Sometimes large open dislocation loops are discovered, as shown in the following micrographs. This is shown in Figure 27, along with a sketch (a) where one can easily have an idea of the implication of these observations. With no regard to the temperature and dose studied, open loops were found in all the specimens, as shown in Figure 27b,c.

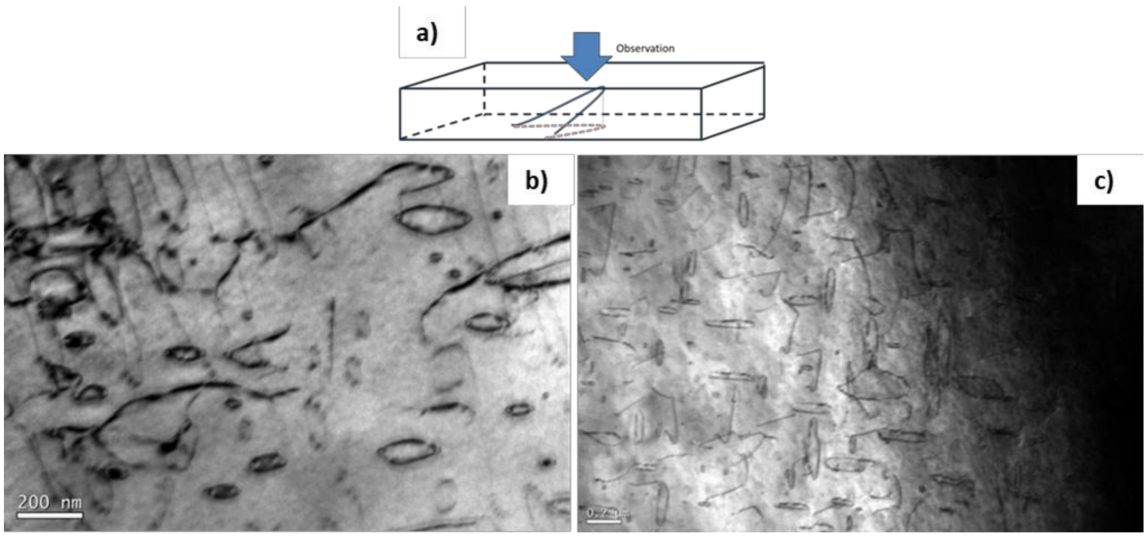


Figure 27. Schematic representation of an open loop (**a**) and TEM micrographs showing open loops distributed within the matrix found at different irradiation conditions (**b**,**c**).

4. Discussion

4.1. Defect Generation during Irradiation

When a vacancy is formed, an interstitial is also formed, but its evolution into more complex defects or recombination depends on many factors. Beyond the initial production of defects, the production bias has significant consequences on the evolution of defects in the irradiated microstructure. One possibility being studied is that, during a cascade, clustered interstitials may move towards relatively close defect sinks due to their high mobility, such as I_2, C_{15}, or developed loops of the $\pm\frac{1}{2}a_0$<111> family in alpha iron [36–39]. This rearrangement would lead to an imbalance between V and I, causing excess vacancies to form vacancies [40] or in some cases, vacancy loops [41,42]. However, in ferritic matrices, they are not usually observed. Similarly, if interstitials form immobile type clusters (or require high energy to move), loops of interstitial dislocations would be generated, which would also act as sinks for other interstitials or mobile clusters of interstitials. This observation has been used to explain [43] the formation of large interstitial loops in irradiated iron [44].

It is well known that the nature of the defect conditions its fate within the environment formed by the crystal and its component defects. In the case of these irradiations in thin foil, among all the loops analysed (showed in the results section), only 5% turned out to be vacancies—of which 4% were detected in the samples at 300 °C, not seeing a clear difference in terms of dose. The identification was quite errant and heterogeneous between the two conditions. It was unfeasible to identify the microstructural features presented in that area that would make forming a vacancy loop the most energetically favourable structure. On the other hand, a similar number of loops, around another 5%, were not univocally identified, also mostly belonging to the 300 °C samples. These results are consistent with the evidence that voids were not detected in all samples. It is possible that some regions had higher concentrations of voids or were closer to one of the two free surfaces acting as a source of these defects. Having detected these loops instead of voids, knowing that the latter is more energetically favourable in Fe BCC [45] may indicate some factor that modifies this bias, which could be the confinement between two relatively close free surfaces. However, it is not very easy to establish a precise correlation in this material, in the same way that vacancy loops occur in other metallic materials such as Zn, Mg, and W [42,46,47]. Nevertheless, the results observed in this investigation agree with the literature.

The damage generated in terms of atomic displacement is relatively low ~10^{-2} dpa, as presented in Figure 3. A low dose generates a low defect density (either loop embryos or already formed loops). This implies that those defects nucleated during irradiation may exist in the material rather than be recombining with defects of opposite nature or interacting with other microstructural features that act as sinks. However, as the dose increases, and thus the atomic damage generated also increases, then the probability of interaction between them increases, generating microstructural evolution [48,49]. If point defects are of the same nature and the energy state is favourable, they will form vacancy and/or interstitial clusters even if their Burger vector is different [50,51]. However, it should be pointed out that these hypotheses are based on computational calculations, as they are experimentally challenging to observe and validate. This evolution strongly depends on the host material and thus on its crystal structure. In the case of BCC iron, either voids, vacancy clusters, or dislocation loops (both V and I) can form.

4.2. Effect of Temperature and Dose on Loop Size

Loops can move in two different ways: glide or climb [52]. The gliding mechanism is the one that occurs in the glide plane and the climbing mode is the one that allows prismatic loops to move in their habit plane. For that movement to occur, vacancies must be absorbed or emitted, allowing that extra partial plane (in the case of interstitial loops) to move. In terms of mobility, both can move within the crystal lattice, although the energy required to move is much lower for $\pm\frac{1}{2}a_0$<111> (glissile) than $\pm a_0$<100> (sessile) in irradiated BCC

iron. However, recent papers supported by computational codes observed that $\pm a_0$<100> loops may have mobility mechanisms more complex than gliding and climbing, such as 1D diffusion changing their habit plane [53], so considering them immobile (sessile) is not entirely correct. On the other hand, it has been shown that C15 clusters [48,54,55] act as embryos of loops since they can evolve into loops with b $\pm a_0$<100> or b $\pm \frac{1}{2} a_0$<111>, or even to more complex forms with the so-called mixed loops [55]. This evolution depends, once again, on certain boundary conditions, namely irradiation temperature, dose, dose rate, and in the present case, the volume of material available to relax [41,56]. If the dose continues to increase, the interaction between defects is enhanced. The population proportionally increases until the rate of generation of new defects slows down, increasing the growth phase until reaching a saturation value that depends on the dose rate and temperature, as long as this is approximately 0.3–0.4 Tm (melting temperature) [57]. This phenomenon becomes even more critical in volumes of material where one of the dimensions is of the same order of magnitude as the defects [30]. As is the case here, the depth, where the foil is almost 100 nm thick, is approximately equivalent to 350 atoms. As the loop grows, its effect as a defect sink also increases, which, from an energetic point of view, implies that its movement through the crystal becomes more complex so that as the irradiation elapses, it becomes an element with which other loops can interact if encountered [58]. This hypothesis reinforces the idea that the growth of dislocation loops will be dominated by the movement and subsequent trapping of minor interstitial-type defects rather than by the reaction of small loops generating a large one, which occurs during cascading overlap [59,60].

The future of a defect produced by irradiation largely depends on the initial stages of the generation of the embryos of that defect. During the cascade of atomic displacements, a huge number of point defects are generated, among which only a few will survive, i.e., they will not recombine with a defect of the opposite nature (vacancy with interstitial), allowing them to form larger defects [61,62]. Similarly, a high rate of defect cluster generation (I_n or V_n) decreases the level of recombination since the population available for recombination decreased. This phenomenon is enhanced when the defect clusters are mobile (glissiles), moving away from the volume of material affected by the cascade. Therefore, the higher the clustering rate is, then the lower the recombination, which means higher strain damage.

Consequently, the material cannot inhibit the formation of such defects with the consequent occurrence of irradiation damage. Specifically, in the case of steels, BCC alloys can withstand irradiation better than those with an FCC crystal structure [63–68]. Evidently, for crystals with the same atomic structure, the resistance to radiation depends on the microstructural characteristics as well as on the composition, i.e., on the binding energy (the energy that must be transferred to a nucleus to be removed from its equilibrium position) [54,60,69].

Therefore, it has been well established that so-called bias effects, e.g., dislocation bias and production bias play an essential role [70] in the process of damage structure evolution in materials subjected to irradiation.

Irrespective of fluence or irradiation temperature, it was shown that the vast majority of the loops were of the $\pm a_0$<100> type, with the $\pm \frac{1}{2} a_0$<111> loops being much smaller in size. To analyse the effect of the dose and temperature as factors promoting the growth or nucleation of loops (which is similar to saying that they enhance the development of pre-loop embryos to small loops), all loops are considered regardless of their habit plane. Figure 28 compares the four experiments by setting the temperature and increasing the dose (a, 300 °C and b, 450 °C) or vice versa (c, low dose, and d, high dose). It is observed that, at low temperatures, an increase in the dose generally causes the growth of the loops and a significant decrease in the population of loops smaller than 100 nm (i.e., if comparing the orange and blue curves, the size distribution tends to larger and a wider range of sizes). This effect is also evident at high temperatures, although a decrease in the population of loops smaller than 100 nm is not as high as that at low temperatures (b). Suppose that the dose value is fixed and the effect of temperature is evaluated. In that case, the effect

produced promotes the generation of medium and small-sized loops, detecting larger loops at higher doses.

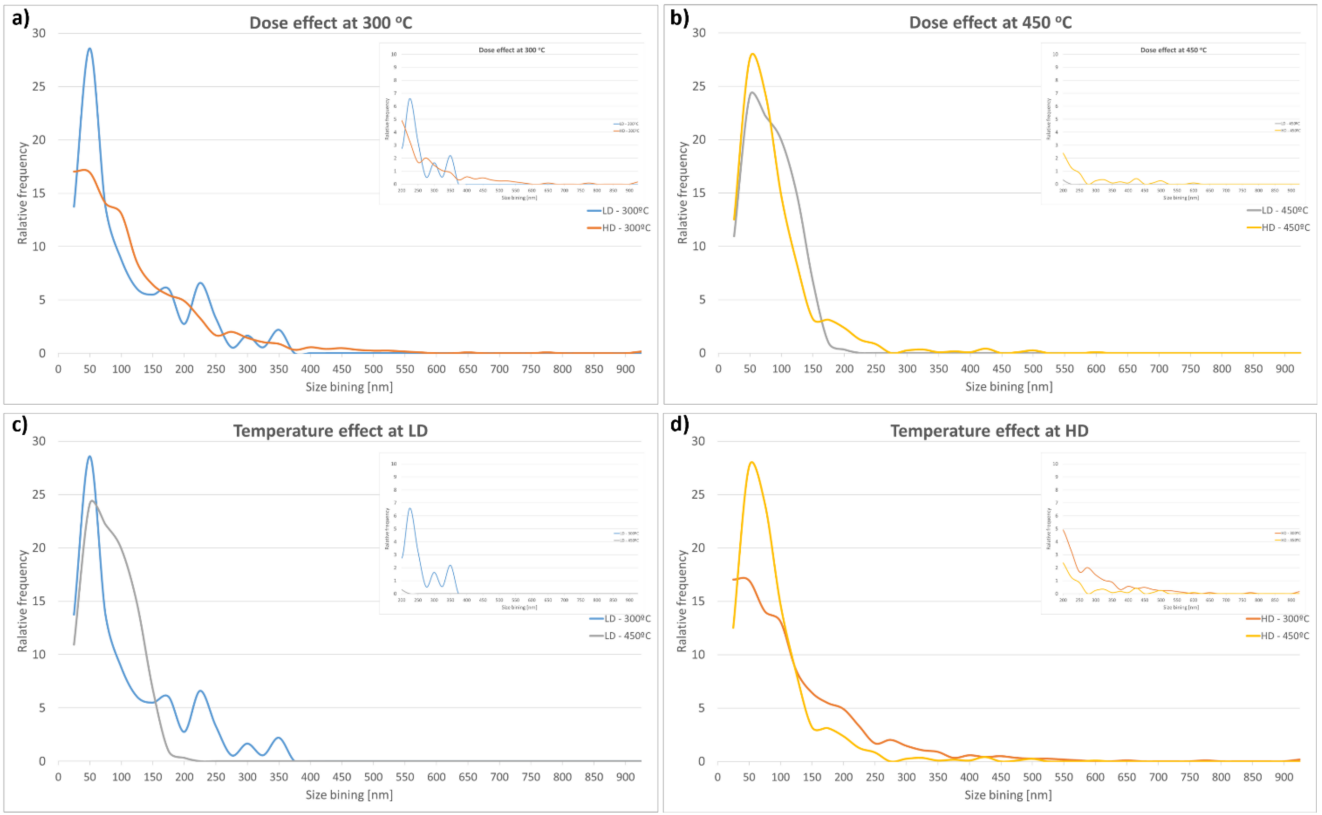


Figure 28. Effect of increasing the irradiation dose at constant temperatures of (**a**) 300 °C; and (**b**) 450 °C, and of increasing the irradiation temperature for the same effective doses—(**c**) low dose; and (**d**) high dose.

It is important to note that this evidence does not discriminate between loops but analyses them to obtain a global picture. A study in which the evolution of loops with habit planes {200} and {111} were studied separately will probably shed better light on this as it is likely that the small mobile loops play a fundamental role in the nucleation and growth of the loops. This has been demonstrated in several papers where they propose possible reactions between different types of loops [71–73], opening the possibility that two loops $\pm\frac{1}{2}a_0$<111> interact with one another, forming a $\pm a_0$<100> loop.

4.3. Burger Vector and Habit Planes

Once we have a global picture of the effect of dose and temperature on the size distribution of the loops, as well as on their distribution density (remembering that this is an average of several micrographs in different areas of the sample, since it is not a completely homogeneous distribution as shown in Figure 17), it was experimentally observed that most of the loops of a size greater than 5 nm are of the $\pm a_0$<100> family.

In the literature, many works have been carried out to obtain in-depth knowledge of the relationship between the chemical composition, the microstructure of the material, and the irradiation characteristics (such as temperature, fluence, dose, or radiant species). In the case of pure iron BCC, in [9,22,44,74], in situ irradiations were performed with Fe ions between 100 and 150 KeV and temperatures between 300 and 500 °C, in the order of 1–2 dpa, concluding that at temperatures below 300 ^{O}C, the $\pm\frac{1}{2}a_0$<111> loops are the majority. As the temperature increases, the population of $\pm a_0$<100> loops increases until they are the only ones detected. In [10], a thin foil was irradiated with 500 keV up to 0.5 dpa at RT, observing that the presence of defects was much higher in the thin foil than

in the bulk material, and that most of the defects were of the $\pm a_0$<100> type. The difference in the observations lies in the ion energy and the effect of interstitials injected into the sample, intervening in the evolution of the defects. For this reason, it is possible that even at temperatures of 300 °C, most of the loops are $\pm\frac{1}{2}a_0$<111>, whereas, in this investigation, the majority were $\pm a_0$<100>. However, it is true that most of the mobile loops $\pm\frac{1}{2}a_0$<111> are detected at lower irradiation temperatures.

In [75], a foil was irradiated with 1 MeV of Kr at 435 °C together with He, achieving damage between 15 and 25 dpa. The observations predicted complex reaction mechanisms, although the expected reaction was that the formed loops would be $\pm\frac{1}{2}a_0$<111> and $\pm a_0$<100>. However, in the initial stages of irradiation with doses of approximately 1 dpa, the size of the loops is notably smaller than those detected in this work; the damage was substantially more significant than that predicted by SRIM with Fe ions at 20 MeV.

Although the comparison is not entirely accurate, experiments with neutrons passing through the sample without depositing interstitials reflect that at low temperatures and doses, most loops are $\pm\frac{1}{2}a_0$<111> (70 °C and 4.7 × 10^{20} n/cm^2 and 0.72 dpa [76], 60 °C and 2.5 × 10^{20} n/cm^2 [77]), while for higher temperatures and doses, most of the observed loops are $\pm a_0$<100> ([78] observed at temperatures between 275 and 450 °C, from 0.87 to 1.13 × 10^{21} n cm^2, [79] at 300 °C, 1.5 × 10^{21} n/cm^2 and 0.2 dpa, [80] at 400 °C, up to a dose of 25.8 dpa, but without giving the fluence in n/cm^2).

4.4. Open Loops and Free Surfaces

On the other hand, the effect of free surfaces and the observed crystal surface orientation must be considered. For example, the glissile dislocation loops $\pm\frac{1}{2}a_0$[111] can be lost on the surface by sliding if the surface is oriented close to the (111) plane. In contrast, in a thin film (110), two variants of $\pm\frac{1}{2}a_0$<111> loops have a Burger vector lying in the plane of the film and cannot be lost by sliding; and for that reason, a higher amount of $\pm\frac{1}{2}a_0$<111> was observed [8].

The proportion of dislocation loops with b $\pm a_0$<200> and $\pm\frac{1}{2}a_0$<111> depends, among other things, on the irradiation temperature: in general, $\pm\frac{1}{2}a_0$<111> loops are preferentially created at low temperatures, while $\pm a_0$<100> loops are preferentially created at high temperatures. In this case, it is impossible to confirm the predominant mechanism that generates such large $\pm a_0$<100> loops and such a low $\pm\frac{1}{2}a_0$<111> density, but it is probably the coalescence of these forming $\pm a_0$<100>, acting in turn as sinks for more defects. Furthermore, in some cases, when the loops are small, such as those referred to as embryos in this work, which are smaller than 5 nm, they are not fully identified, although they are estimated to be of the $\pm\frac{1}{2}a_0$<111> type [81]. Similar observations on the effect of crystal surface orientation were obtained in [11].

4.5. Nature of Loops (Vacancy or Interstitial)

Interstitials, as well as vacancies, can form the dislocation loops generated by irradiation. Those of interstitial type, as is evident, produce a higher distortion in the crystal structure, generating larger elastic fields of strain so that the interaction with other defects is more significant, acting as defect sinks. This observation indicates that the loops prefer interstitial defects to vacancies, modifying the final resulting microstructure of the crystal. The bias induced by a dislocation depends on the magnitude of its Burgers vector, so in principle, $\pm\frac{1}{2}a_0$<111> type loops will have a higher capture efficiency than $\pm a_0$<100> loops. Despite this, a new work has obtained results which highlight that this phenomenon is not so straightforward [82]. The experimental procedure section described in detail that the empirical determination of the nature of dislocation loops is a complex task [83,84].

Although loops of the two types can form with both b $\pm\frac{1}{2}a_0$<111> and $\pm a_0$<100>, those formed of vacancies are not usually detected since vacancies have a higher migration energy than interstitials within a crystal [85]. Moreover, they tend to cluster together, leading to the forming of voids and the consequent swelling effect [86,87]. On the other hand, to a lesser extent, a sink effect was observed in all samples in grain boundaries, as

shown in Figure 29. The mechanism at work was explained in [88], which allows predicting a recombination of defects in the vicinity of these features. However, the authors did not go into detail about the possible effect of crystal misorientation, and therefore, omitted details of the relationship between the energy of the grain boundary and its potential as a defect sink.

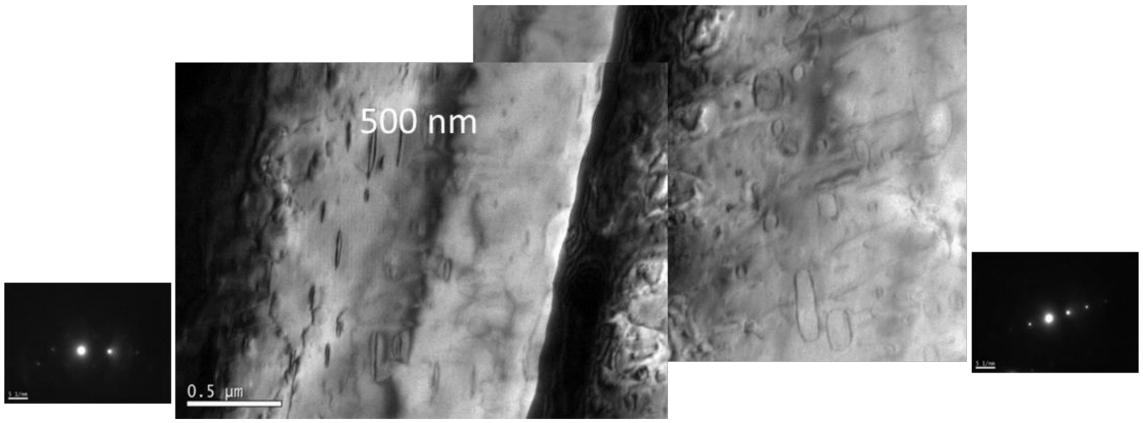


Figure 29. Irradiation sink effect at a grain boundary.

The Fresnel contrast revealed vacancy-type structures <5 nm in diameter which were randomly distributed throughout the lamellae for all alloys; however, it could not be verified whether they were not simply oxides on the sample surface, so they were not analysed.

Available studies have shown that most of the dislocation loops created under irradiation in pure Fe are of interstitial type, as shown by TEM on samples irradiated with different species [78,89,90].

5. Conclusions

- Apparent differences were found between thin foil irradiation and the first nm in bulk specimens in terms of dislocation loops. There is an evident effect of the reduced volume available for the defects to recombine in thin-film specimens.
- Understanding the complex diffusion mechanism of $\pm a_0$<100> loops is a critical step in further exploring the mechanical properties of Fe and Fe-based alloys associated with the formation of $\pm a_0$<100> dislocation loops by deformation or radiation.
- Most of the loops identified in all four experimental conditions were b $\pm a_0$<100> type, between 80% and 92% in total. With regard to the literature, those dislocations at 300 °C should be $\pm\frac{1}{2}a_0$<111>, and as the irradiation temperature increases, should also be the $\pm a_0$<100> loop population. However, in this research, the observations indicated otherwise.
- The highest average loop size value was found for HD 300 °C, and the largest loop, 907 nm, corresponded to nine times the sample thickness. In addition, this experimental condition produced the biggest loop swelling, 0.14%.
- Free surfaces orientation must be taken into consideration to determine the importance of this parameter in terms of defect annihilation or image forces.

Author Contributions: M.R.: conceptualisation, methodology, investigation, formal analysis, writing—original draft preparation, and writing—review and editing; F.J.S.: methodology, investigation, and writing—review and editing; P.F.: conceptualisation and supervision; C.J.O.: software and validation; A.G.-H.: methodology and formal analysis; and D.J.R.: methodology. All authors have read and agreed to the published version of the manuscript.

Funding: This research was funded by Spanish CM, TECHNOFUSION III- CM (2018/EMT-4437) and MICINN project PID2019-105325RB-C31. This work was carried out within the framework of the

EUROfusion Consortium and received funding from the Euratom research and training programme 2014–2018 and 2019–2020 under grant agreement No 633053. The views and opinions expressed herein do not necessarily reflect those of the European Consortium.

Institutional Review Board Statement: Not applicable.

Informed Consent Statement: Not applicable.

Acknowledgments: The authors want to acknowledge ELECMI (at Madrid, CNME, and Zaragoza, LMA) and CMAM staff for their outstanding work and support, and Natalia Willey Toledo for her help with language editing, improving the paper quality.

Conflicts of Interest: The authors declare no conflict of interest.

References

1. Knaster, J. An assessment of the available alternatives for fusion relevant neutron sources. *Nucl. Fusion* **2018**, *58*, 095001. [CrossRef]
2. Haley, J.C.; Briggs, S.A.; Edmondson, P.D.; Sridharan, K.; Roberts, S.G.; Lozano-Perez, S.; Field, K.G. Dislocation loop evolution during in-situ ion irradiation of model FeCrAl alloys. *Acta Mater.* **2017**, *136*, 390–401. [CrossRef]
3. Kaoumi, D.; Adamson, J.; Kirk, M. Microstructure evolution of two model ferritic/martensitic steels under in situ ion irradiation at low doses (0–2dpa). *J. Nucl. Mater.* **2014**, *445*, 12–19. [CrossRef]
4. Kaoumi, D.; Adamson, J. Self-ordered defect structures in two model F/M steels under in situ ion irradiation. *J. Nucl. Mater.* **2014**, *448*, 233–238. [CrossRef]
5. Yang, Z.; Sakaguchi, N.; Watanabe, S.; Kawai, M. Dislocation Loop Formation and Growth under In Situ Laser and/or Electron Irradiation. *Sci. Rep.* **2011**, *1*, 190. [CrossRef] [PubMed]
6. Birtcher, R.; Kirk, M.; Furuya, K.; Lumpkin, G.; Ruault, M.-O. In situ Transmission Electron Microscopy Investigation of Radiation Effects. *J. Mater. Res.* **2005**, *20*, 1654–1683. [CrossRef]
7. Kirk, M.A.; Baldo, P.M.; Liu Amelia, C.Y.; Ryan, E.A.; Birtcher, R.C.; Yao, Z.; Xu, L.S.; Jenkins, M.M.; Hernandez-Mayoral, D.; Kaoumi, T.; et al. In situ transmission electron microscopy and ion irradiation of ferritic materials. *Microsc. Res. Tech.* **2009**, *72*, 182–186. [CrossRef]
8. Jenkins, M.L.; Yao, Z.; Hernández-Mayoral, M.; Kirk, M.A. Dynamic observations of heavy-ion damage in Fe and Fe-Cr alloys. *J. Nucl. Mater.* **2009**, *389*, 197–202. [CrossRef]
9. Yao, Z.; Jenkins, M.L.; Hernández-Mayoral, M.; Kirk, M.A. The temperature dependence of heavy-ion damage in iron: A microstructural transition at elevated temperatures. *Philos. Mag.* **2010**, *90*, 4623–4634. [CrossRef]
10. Prokhodtseva, A.; Décamps, B.; Schäublin, R. Comparison between bulk and thin foil ion irradiation of ultra high purity Fe. *J. Nucl. Mater.* **2013**, *442* (Suppl. 1), S786–S789. [CrossRef]
11. Prokhodtseva, A.; Décamps, B.; Ramar, A.; Schäublin, R. Impact of He and Cr on defect accumulation in ion-irradiated ultrahigh-purity Fe(Cr) alloys. *Acta Mater.* **2013**, *61*, 6958–6971. [CrossRef]
12. Roldán, M.; Fernández, P.; Rams, J.; Jiménez-Rey, D.; Materna-Morris, E.; Klimenkov, M. Comparative study of helium effects on EU-ODS EUROFER and EUROFER97 by nanoindentation and TEM. *J. Nucl. Mater.* **2015**, *460*, 226–234. [CrossRef]
13. Chen, J.; Duval, F.; Jung, P.; Schäublin, R.; Gao, N.; Barthe, M.-F. Dislocation loops in ultra-high purity Fe(Cr) alloys after 7.2 MeV proton irradiation. *J. Nucl. Mater.* **2018**, *503*, 81–90. [CrossRef]
14. Nordlund, K.; Zinkle, S.J.; Sand, A.E.; Granberg, F.; Averback, R.S.; Stoller, R.E.; Suzudo, T.; Malerba, L.; Banhart, F.; Weber, W.J.; et al. Primary radiation damage: A review of current understanding and models. *J. Nucl. Mater.* **2018**, *512*, 450–479. [CrossRef]
15. Fikar, J.; Gröger, R. Interactions of prismatic dislocation loops with free surfaces in thin foils of body-centered cubic iron. *Acta Mater.* **2015**, *99*, 392–401. [CrossRef]
16. Stoller, R. The effect of free surfaces on cascade damage production in iron. *J. Nucl. Mater.* **2002**, *307–311*, 935–940. [CrossRef]
17. Korchuganov, A.V.; Zolnikov, K.P.; Kryzhevich, D.S.; Psakhie, S.G. Primary Ion-Irradiation Damage of BCC-Iron Surfaces. *Russ. Phys. J.* **2017**, *60*, 170–174. [CrossRef]
18. Knaster, J.; Moeslang, A.; Muroga, T. Materials research for fusion. *Nat. Phys.* **2016**, *12*, 424–434. [CrossRef]
19. Tan, L.; Snead, L.; Katoh, Y. Development of new generation reduced activation ferritic-martensitic steels for advanced fusion reactors. *J. Nucl. Mater.* **2016**, *478*, 42–49. [CrossRef]
20. Fernández, P.; Hoffmann, J.; Rieth, M.; Roldán, M.; Gómez-Herrero, A. TEM characterisation on new 9% Cr advanced steels thermomechanical treated after tempering. *J. Nucl. Mater.* **2018**, *500*, 1–10. [CrossRef]
21. Roldán, M.; Galán, P.; Sánchez, F.J.; García-Cortés, I.; Jiménez-Rey, D.; Fernández, P. *Ion Beam Experiments to Emulate Nuclear Fusion Environment on Structural Materials at CMAM*; IntechOpen: London, UK, 2018.
22. Jenkins, M.L.; Yao, Z.; Hernández-Mayoral, M.; Kirk, M.A. Direct in-situ electron microscope observations of the dynamics of irradiation damage effects in Fe and FeCr alloys. *J. Nucl. Mater.* **2009**, *389*, 197–202. [CrossRef]
23. Le Coze, J. *Procurement of Pure Fe Metal and Fe-Based Alloys with Controlled Chemical Alloying Element Contents and Microstructure*; Final Report on Model Alloy Preparation; Armines Ecole Nationale Superieure des Mines: Saint Etienne, France, 2007.

24. Roldán, M.; Fernández, P.; Vila, R.; Gómez-Herrero, A.; Sánchez, F.J. The effect of triple ion beam irradiation on cavity formation on pure EFDA iron. *J. Nucl. Mater.* **2016**, *479*, 100–111. [CrossRef]
25. Saavedra, R.; Jiménez-Rey, D.; Martin, P.; Vila, R. Ionoluminescence of fused silica under swift ion irradiation. *Nucl. Instrum. Methods Phys. Res. Sect. B* **2016**, *382*, 96–100. [CrossRef]
26. Stoller, R.E.; Toloczko, M.B.; Was, G.S.; Certain, A.G.; Dwaraknath, S.; Garner, F.A. On the use of SRIM for computing radiation damage exposure. *Nucl. Instrum. Methods Phys. Res. Sect. B* **2013**, *310*, 75–80. [CrossRef]
27. Kato, N.I. Reducing focused ion beam damage to transmission electron microscopy samples. *J. Electron Microsc.* **2004**, *53*, 451–458. [CrossRef] [PubMed]
28. Howie, A.; Whelan, M.J. Diffraction contrast of electron microscope images of crystal lattice defects. III. Results and experimental confirmation of the dynamical theory of dislocation image contrast. *Proc. R. Soc. Lond. Ser. A Math. Phys. Sci.* **1962**, *267*, 206–230.
29. Yao, B.; Edwards, D.J.; Kurtz, R.J. TEM characterisation of dislocation loops in irradiated bcc Fe-based steels. *J. Nucl. Mater.* **2013**, *434*, 402–410. [CrossRef]
30. Qing, L. An equation to determine the practical tilt angle of a double-tilt specimen holder and its application to transmission electron microscopy. *Micron Microsc. Acta* **1989**, *20*, 261–264. [CrossRef]
31. Maher, D.M.; Eyre, B.L. Neutron irradiation damage in molybdenum. *Philos. Mag.* **1971**, *23*, 409–438. [CrossRef]
32. Eyre, B.L.; Perrin, R.C.; Maher, D.M. Electron microscope image contrast from small dislocation loops. I. Theoretical predictions for edge dislocation loops in a BCC crystal. *J. Phys. F Met. Phys.* **1977**, *7*, 1359–1369. [CrossRef]
33. Williams, D.B.; Barry, C.C. *Transmission Electron Microscopy: A Textbook for Materials*; Springer: Berlin/Heidelberg, Germany, 2009; p. 779.
34. Robinson, M.T.; Torrens, I.M. Computer simulation of atomic-displacement cascades in solids in the binary-collision approximation. *Phys. Rev. B* **1974**, *12*, 5008–5024. [CrossRef]
35. Robinson, M.T. Slowing-down time of energetic atoms in solids. *Phys. Rev. B* **1989**, *40*, 10717–10726. [CrossRef]
36. Broeders, C.; Konobeyev, A. Defect production efficiency in metals under neutron irradiation. *J. Nucl. Mater.* **2004**, *328*, 197–214. [CrossRef]
37. Domain, C.; Becquart, C.S. Ab initio calculations of defects in Fe and dilute Fe-Cu alloys. *Phys. Rev. B* **2001**, *65*, 024103. [CrossRef]
38. Willaime, C.-C.F.F.; Ordejón, P. Stability and Mobility of Mono- and Di-Interstitials in alpha-Fe. *Phys. Rev. Lett.* **2004**, *92*, 175503.
39. Fu, C.-C.; Torre, J.D.; Willaime, F.; Bocquet, J.-L.; Barbu, A. Multiscale modelling of defect kinetics in irradiated iron. *Nat. Mater.* **2004**, *4*, 68–74. [CrossRef]
40. Heald, P.T. The preferential trapping of interstitials at dislocations. *Philos. Mag. J. Theor. Exp. Appl. Phys.* **1975**, *31*, 551–558. [CrossRef]
41. Aliaga, M.; Schäublin, R.; Löffler, J.F.; Caturla, M. Surface-induced vacancy loops and damage dispersion in irradiated Fe thin films. *Acta Mater.* **2015**, *101*, 22–30. [CrossRef]
42. Hales, R.; Smallman, R.E.; Dobson, P.S. The Formation and Growth of Vacancy Loops in Magnesium. *Proc. R. Soc. Lond. Ser. A Math. Phys. Sci.* **1968**, *307*, 71–81.
43. Terentyev, D.A.; Klaver, T.P.C.; Olsson, P.; Marinica, M.-C.; Willaime, F.; Domain, C.; Malerba, L. Self-Trapped Interstitial-Type Defects in Iron. *Phys. Rev. Lett.* **2008**, *100*, 145503. [CrossRef]
44. Hernández-Mayoral, M.; Yao, Z.; Jenkins, M.; Kirk, M. Heavy-ion irradiations of Fe and Fe-Cr model alloys Part 2: Damage evolution in thin-foils at higher doses. *Philos. Mag.* **2008**, *88*, 2881–2897. [CrossRef]
45. Gilbert, M.; Dudarev, S.L.; Derlet, P.M.; Pettifor, D.G. Structure and metastability of mesoscopic vacancy and interstitial loop defects in iron and tungsten. *J. Phys. Condens. Matter* **2008**, *20*, 345214. [CrossRef]
46. Dai, C.; Long, F.; Saidi, P.; Béland, L.K.; Yao, Z.; Daymond, M.R. Primary damage production in the presence of extended defects and growth of vacancy-type dislocation loops in hcp zirconium. *Phys. Rev. Mater.* **2019**, *3*, 043602. [CrossRef]
47. Fikar, J.; Schäublin, R.; Mason, D.R.; Nguyen-Manh, D. Nano-sized prismatic vacancy dislocation loops and vacancy clusters in tungsten. *Nucl. Mater. Energy* **2018**, *16*, 60–65. [CrossRef]
48. Byggmästar, J.; Granberg, F. Dynamical stability of radiation-induced C15 clusters in iron. *J. Nucl. Mater.* **2019**, *528*, 151893. [CrossRef]
49. Granberg, F.; Byggmästar, J.; Nordlund, K. Defect accumulation and evolution during prolonged irradiation of Fe and FeCr alloys. *J. Nucl. Mater.* **2019**, *528*, 151843. [CrossRef]
50. Arakawa, K.; Amino, T.; Mori, H. Direct observation of the coalescence process between nanoscale dislocation loops with different Burgers vectors. *Acta Mater.* **2011**, *59*, 141–145. [CrossRef]
51. Grammatikopoulos, P.; Bacon, D.J.; Osetsky, Y.N. Simulation of the interaction between an edge dislocation and ⟨111⟩ interstitial dislocation loops in α-iron. *Radiat. Eff. Defects Solids* **2019**, *174*, 329–338. [CrossRef]
52. Hull, D.; Bacon, D.J. *Introduction to Dislocations*; Elsevier: Amsterdam, The Netherlands, 2011.
53. Gao, N.; Yao, Z.W.; Lu, G.H.; Deng, H.Q.; Gao, F. Mechanisms for interstitial dislocation loops to diffuse in BCC iron. *Nat. Commun.* **2021**, *12*, 225. [CrossRef]
54. Alexander, R.; Proville, L.; Becquart, C.S.; Goryeava, A.M.; Dérès, J.; Lapointe, C.; Marinica, M.C. Interatomic potentials for irradiation-induced defects in iron. *J. Nucl. Mater.* **2020**, *535*, 152141. [CrossRef]
55. Byggmästar, J.; Granberg, F.; Sand, A.E.; Pirttikoski, A.; Alexander, R.; Marinica, M.-C.; Nordlund, K. Collision cascades overlapping with self-interstitial defect clusters in Fe and W. *J. Phys. Condens. Matter* **2019**, *31*, 245402. [CrossRef]

56. Stoller, R.E. The role of cascade energy and temperature in primary defect formation in iron. *J. Nucl. Mater.* **2000**, *276*, 22–32. [CrossRef]
57. Zinkle, S.J. Microstructures and mechanical properties of irradiated metals and alloys. In *Materials Issues for Generation IV Systems*; Ghetta, D.V., Gorse, D.M., Pontikis, V., Eds.; Springer: Berlin/Heidelberg, Germany, 2008; pp. 227–244.
58. Li, Y.; Boleininger, M.; Robertson, C.; Dupuy, L.; Dudarev, S.L. Diffusion and interaction of prismatic dislocation loops simulated by stochastic discrete dislocation dynamics. *Phys. Rev. Mater.* **2019**, *3*, 073805. [CrossRef]
59. Jenkins, M.; Kirk, M.; Phythian, W. Experimental studies of cascade phenomena in metals. *J. Nucl. Mater.* **1993**, *205*, 16–30. [CrossRef]
60. Souidi, A.; Hou, M.; Becquart, C.S.; Domain, C. Atomic displacement cascade distributions in iron. *J. Nucl. Mater.* **2001**, *295*, 179–188. [CrossRef]
61. Kirk, M.; Robertson, I.; Vetrano, J.; Jenkins, M.; Funk, L. *The Collapse of Defect Cascades to Dislocation Loops during Self-Ion Irradiations of Iron, Nickel, and Copper at 30, 300, and 600 K*; ASTM: West Conshohocken, PA, USA, 1987.
62. Kim, Y.S. Primary radiation damage characterisation of α-iron under irradiation temperature for various PKA energies. *Mater. Res. Express* **2018**, *5*, 046518.
63. Straalsund, J.; Powell, R.; Chin, B. An overview of neutron irradiation effects in LMFBR materials. *J. Nucl. Mater.* **1982**, *108–109*, 299–305. [CrossRef]
64. Brailsford, A.; Mansur, L. Effect of self-ion injection in simulation studies of void swelling. *J. Nucl. Mater.* **1977**, *71*, 110–116. [CrossRef]
65. Cawthorne, C.; Fulton, E.J. Voids in Irradiated Stainless Steel. *Nature* **1967**, *216*, 575–576. [CrossRef]
66. Garner, F.A. Radiation-induced damage in austenitic structural steels used in nuclear reactors. In *Comprehensive Nuclear Materials*, 2nd ed.; Konings, R.J.M., Stoller, R.E., Eds.; Elsevier: Amsterdam, The Netherlands, 2020; pp. 57–168.
67. Hashimoto, N.; Kasada, R.; Raj, B.; Vijayalakshmi, M. Radiation effects in ferritic steels and advanced ferritic-martensitic steels. In *Comprehensive Nuclear Materials*, 2nd ed.; Konings, R.J.M., Stoller, R.E., Eds.; Elsevier: Amsterdam, The Netherlands, 2020; pp. 226–254.
68. Golubov, S.; Singh, B.; Trinkaus, H. Defect accumulation in fcc and bcc metals and alloys under cascade damage conditions—Towards a generalisation of the production bias model. *J. Nucl. Mater.* **2000**, *276*, 78–89. [CrossRef]
69. Becquart, C.S.; Domain, C.; Legris, A.; van Duysen, J.C. Influence of the interatomic potentials on molecular dynamics simulations of displacement cascades. *J. Nucl. Mater.* **2000**, *280*, 73–85. [CrossRef]
70. Kuramoto, E.; Ohsawa, K.; Imai, J.; Obata, K.; Tsutsumi, T. Bias Mechanism and Its Effects for Fundamental Process of Irradiation Damage. *Mater. Trans.* **2004**, *45*, 34–39. [CrossRef]
71. Swinburne, T.D.; Arakawa, K.; Mori, H.; Yasuda, H.; Isshiki, M.; Mimura, K.; Uchikoshi, M.; Dudarev, S.L. Fast, vacancy-free climb of prismatic dislocation loops in bcc metals. *Sci. Rep.* **2016**, *6*, 30596. [CrossRef] [PubMed]
72. Arakawa, K.; Amino, T.; Yasuda, H.; Mori, H. <110>Dislocation Junction Formation via the Coalescence between Nanoscale 1/2 <111> Prismatic Dislocation Loops in Iron. *ISIJ Int.* **2017**, *57*, 2065–2069. [CrossRef]
73. Xu, H.; Stoller, R.E.; Osetsky, Y.N.; Terentyev, D. Solving the Puzzle of ⟨100⟩ Interstitial Loop Formation in bcc Iron. *Phys. Rev. Lett.* **2013**, *110*, 265503. [CrossRef]
74. Yao, Z.; Hernández-Mayoral, M.; Jenkins, M.L.; Kirk, M.A. Heavy-ion irradiations of Fe and Fe-Cr model alloys Part 1: Damage evolution in thin-foils at lower doses. *Philos. Mag.* **2008**, *88*, 2851–2880. [CrossRef]
75. Lin, Y.-R.; Chen, W.-Y.; Li, M.; Henry, J.; Zinkle, S.J. Dynamic observation of dual-beam irradiated Fe and Fe-^{10}Cr alloys at 435 °C. *Acta Mater.* **2021**, *209*, 116793. [CrossRef]
76. Zinkle, S.; Singh, B. Microstructure of neutron-irradiated iron before and after tensile deformation. *J. Nucl. Mater.* **2006**, *351*, 269–284. [CrossRef]
77. Eyre, B.L.; Bartlett, A.F. An electron microscope study of neutron irradiation damage in alpha-iron. *Philos. Mag. J. Theor. Exp. Appl. Phys.* **1965**, *12*, 261–272. [CrossRef]
78. Horton, L.L.; Bentley, J.; Farrell, K. TEM study of neutron-irradiated iron. *J. Nucl. Mater.* **1982**, *108–109*, 222–233. [CrossRef]
79. Matijasevic, M.; van Renterghem, W.; Almazouzi, A. Characterisation of irradiated single crystals of Fe and Fe-15Cr. *Acta Mater.* **2009**, *57*, 1577–1585. [CrossRef]
80. Konobeev, Y.V.; Dvoriashin, A.M.; Porollo, S.I.; Garner, F.A. Garner, Swelling and microstructure of pure Fe and Fe-Cr alloys after neutron irradiation to ∼26 dpa at 400 °C. *J. Nucl. Mater.* **2006**, *355*, 124–130. [CrossRef]
81. Hernández-Mayoral, M.; Gómez-Briceño, D. Transmission electron microscopy study on neutron irradiated pure iron and RPV model alloys. *J. Nucl. Mater.* **2010**, *399*, 146–153. [CrossRef]
82. Chang, Z.; Terentyev, D.; Sandberg, N.; Samuelsson, K.; Olsson, P. Anomalous bias factors of dislocations in bcc iron. *J. Nucl. Mater.* **2015**, *461*, 221–229. [CrossRef]
83. Loretto, M.H. *Electron Beam Analysis of Materials*; Springer: Berlin/Heidelberg, Germany, 1984.
84. Kirk, M.; Yi, X.; Jenkins, M. Characterisation of irradiation defect structures and densities by transmission electron microscopy. *J. Mater. Res.* **2015**, *30*, 1195–1201. [CrossRef]
85. Johnson, R.A. Interstitials and Vacancies in α Iron. *Phys. Rev.* **1964**, *134*, A1329–A1336. [CrossRef]
86. Surh, M.P.; Sturgeon, J.B.; Wolfer, W.G. Void nucleation, growth, and coalescence in irradiated metals. *J. Nucl. Mater.* **2008**, *378*, 86–97. [CrossRef]

87. Cottrell, G.A. Void migration, coalescence and swelling in fusion materials. *Fusion Eng. Design* **2003**, *66–68*, 253–257. [CrossRef]
88. Li, X.; Liu, W.; Xu, Y.; Liu, C.; Pan, B.; Liang, Y.; Fang, Q.; Chen, J.-L.; Luo, G.-N.; Lu, G.-H.; et al. Energetic and kinetic dataset on interaction of the vacancy and self-interstitial atom with the grain boundary in α-iron. *Data Brief.* **2016**, *7*, 798–813. [CrossRef] [PubMed]
89. Robertson, I.M.; Jenkins, M.L.; English, C.A. Low-dose neutron-irradiation damage in alfa iron. *J. Nucl. Mater.* **1982**, *108*, 12.
90. Marian, J.; Wirth, B.D.; Schäublin, R.; Perlado, J.M.; de la Rubia, T.D. <100>-Loop characterisation in α-Fe: Comparison between experiments and modeling. *J. Nucl. Mater.* **2002**, *307*, 871–875. [CrossRef]